# Molecular factors determining brightness in fluorescence-encoded infrared vibrational spectroscopy

Abhirup Guha,[1,a] Lukas Whaley-Mayda,[1] Seung Yeon Lee,[1] and Andrei Tokmakoff[1]

*Department of Chemistry, James Franck Institute, and Institute of Biophysical Dynamics,*

*The University of Chicago, Chicago, Illinois 60637, USA*

Fluorescence-encoded infrared (FEIR) spectroscopy is a recently developed technique for solution-phase vibrational spectroscopy with detection sensitivity at the single-molecule level. While its spectroscopic information content and important criteria for its practical experimental optimization have been identified, a general understanding of the electronic and nuclear properties required for highly sensitive detection, i.e., what makes a molecule a "good FEIR chromophore", is lacking. This work explores the molecular factors that determine FEIR vibrational activity and assesses computational approaches for its prediction. We employ density functional theory (DFT) and its time-dependent version (TD-DFT) to compute vibrational and electronic transition dipole moments, their relative orientation, and the Franck-Condon factors involved in FEIR activity. We apply these methods to compute the FEIR activities of normal modes of chromophores from the coumarin family and compare these predictions with experimental FEIR cross-sections. We discuss the extent to which we can use the computational models to predict FEIR activity of individual vibrations in a candidate molecule. The results discussed in this work provide the groundwork for computational strategies for choosing FEIR vibrational probes or informing the structure of designer chromophores for single-molecule spectroscopic applications.

[a)] Author to whom correspondence should be addressed: abhirupg@uchicago.edu

# I. INTRODUCTION

Infrared (IR) and Raman vibrational spectroscopies enable studies of chemical structure and dynamics with molecular information at the length scale of chemical bonds. However, conventional implementations suffer from poor detection sensitivity and are limited to ensemble-averaged measurements in high-concentration samples. Many strategies to increase detection sensitivity have been developed, bringing vibrational methods into the single-molecule (SM) regime. The primary path towards SM vibrational spectroscopy was paved with the development of surface-enhanced Raman spectroscopy and related methods, [1-3] [4,16,17] which exploit local surface plasmon resonance to enhance the vibrational Raman interaction, and are now mainstream tools in SM science. However, the requirement of placing the molecule at a metallic interface makes these and other plasmonically-enhanced approaches difficult to apply for systems requiring a native solution-phase environment.

Alternative approaches to improve the sensitivity of vibrational spectroscopy by coupling IR absorption or Raman pumping to fluorescence emission avoid the need for plasmonic enhancement, and have origins pre-dating SM spectroscopy.[5-8] These methods benefit from the advantages of fluorescence in achieving sensitive detection in a wide variety of molecular environments.[9-12] For example, Min and co-workers have demonstrated SM detection with stimulated Raman excited fluorescence (SREF) spectroscopy, enabling SM Raman vibrational bioimaging.[13-15] We have introduced fluorescence-encoded infrared (FEIR) spectroscopy, which operates by up-converting ("encoding") an IR-pumped vibrational excited state into a fluorescent electronic excited state by subsequent absorption of a visible photon (Fig. 1).[5-7,16-19] Our implementation of FEIR spectroscopy incorporates high repetition-rate, femtosecond pulsed excitation with confocal microscopy and single-photon counting to achieve SM sensitivity in solution.[17] Recently, Wei and co-workers have adapted the same principle with higher repetition-rate excitation and narrowband picosecond IR pulses, and demonstrated SM IR-vibrational imaging.[20] A related approach that also utilized plasmonic enhancement with continuous-wave excitation was recently demonstrated by Baumberg and co-workers to achieve SM detection.[21]

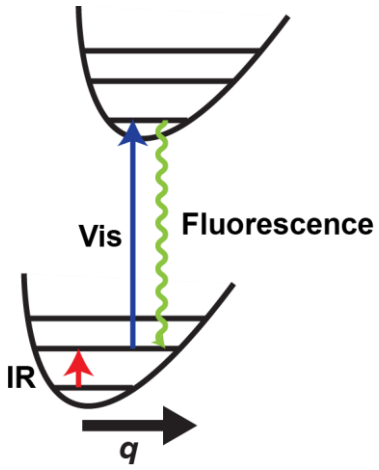


**FIG. 1.** Level diagram illustrating the IR + visible sequential excitation and subsequent fluorescence emission involved in FEIR spectroscopy.

Understanding the molecular factors involved in overall detection sensitivity is critical for developing SM applications of FEIR spectroscopy. At its basic level this amounts to determining "FEIR selection rules", or the conditions required of a particular vibrational mode for producing a strong FEIR signal. SM-capable FEIR chromophores should be bright and stable fluorophores, with target vibrations of strong IR activity. For example, common organic fluorophores like cyanines, coumarins, xanthenes, and acridines have intense electronic transitions with IR-bright skeletal ring vibrations in the 6 μm region, and may serve as a pool for selecting promising FEIR candidates. Importantly, the encoding step also requires vibronic coupling, and we therefore expect Franck-Condon activity of the target vibrations to be a crucial factor. Another aspect of FEIR chromophore selection involves the identification of useful target vibrations that can act as "probes" of chemical interactions or structure changes, e.g. carbonyl or nitrile stretching modes. Such reporter modes must also be sufficiently FEIR-bright for SM applications.

These considerations provide guidelines and a starting point for identifying candidate chromophores. However, while some of these parameters—for instance electronic spectra, absorption cross-sections, and fluorescence quantum yields—are widely available across many dye families, many are not or are difficult to determine experimentally. Specifically, vibronic couplings are in general difficult to measure with conventional spectroscopic characterization tools. This motivates the development of robust and straightforward computational approaches to predict FEIR brightness.

In this work, we explore the molecular factors that control FEIR brightness and test the ability of electronic structure methods to predict them. We propose a simple theoretical construct of a vibration's FEIR activity based on the underlying matrix elements of the molecular transitions involved that is readily

computed from density function theory (DFT) structure calculations. We perform calculations across a series of coumarins, a well-established dye family whose electronic spectra can be tuned by intramolecular charge transfer manifested through a push-pull mechanism exerted by the substituents on the coumarin core.[22-24] The FEIR activity predictions of these calculations are then correlated against experimental FEIR measurements we have reported previously.[18] One difficulty in comparing the calculated FEIR activities with our experiments is the presence of vibrational coherence dynamics and other time-dependent phenomena in our measurements that arise from using broadband femtosecond excitation pulses. To account for some of these effects, we employ finite-pulse response function simulations developed previously to calculate spectra from the DFT-calculated quantities,[34,35] facilitating a more incisive test of the computational approach.

This paper is organized as follows. Section II describes the theoretical construct of FEIR activity for harmonic vibrations. Section III describes the computational approach we take to calculate these values, and experimental methods for performing FEIR measurements. Section IV provides a detailed discussion on the calculations of the molecular factors determining the FEIR activity for coumarin 6, followed by a comparative study of calculated FEIR activities and experimental FEIR signal strength of normal modes across the series of ten coumarins used in our study. Section V summarizes our conclusions.

# II. THEORY

## A. FEIR activity

We have recently described a nonlinear response function theory for FEIR spectroscopy which models experimental signals via the $4^{th}$-order population of the fluorescent electronic excited state, and accounts for vibrational population and coherence dynamics, vibrational-electronic coupling and dipole orientation, and finite excitation pulses.[25, 26] This theory identifies the relevant molecular transitions and provides a framework for calculating spectra from their matrix elements and the system's dynamics, but involves substantial complexity. To predict a molecule's suitability for FEIR detection, we instead seek a minimal description of the relevant molecular factors amenable to quantum chemical calculation. To this end, here we motivate the construct of FEIR activity as a simple theoretical indicator of the strength of a molecular vibration's FEIR response.

Working in the Born-Oppenheimer approximation, we assume the system is initially in its global ground state $|g, \mathbf{0}\rangle = |g\rangle|\mathbf{0}\rangle$, where $|g\rangle$ is the ground state electronic wavefunction and $|\mathbf{0}\rangle$ denotes the vibrational wavefunction with zero quanta of excitation in each vibrational mode. The bold notation denotes

a vector. This implies, for a molecule with $N$ vibrations, $|\mathbf{0}\rangle$ is an $N$-dimensional product state. Resonant IR excitation promotes one of the vibrations ($j$) to its first excited state $|g,\mathbf{1}_j\rangle = |g\rangle|\mathbf{1}_j\rangle$, where $|\mathbf{1}_j\rangle$ represents an $N$-dimensional product state, where the $j^{th}$ vibration is in the first excited state while the remaining $N-1$ vibrations are in the ground vibrational state. The transition probability for this step is proportional to the square of the vibrational transition dipole moment $\left|\langle 0_j|\mu|1_j\rangle\right|^2 = \left|\mu_j\right|^2$.

The visible encoding pulse subsequently promotes the system to the first excited electronic state with all vibrations in their respective ground states, $|e,\mathbf{0'}\rangle = |e\rangle|\mathbf{0'}\rangle$. A prime ($'$) is used to indicate vibrations on the excited electronic state. We restrict our analysis to transitions arriving in this zero-quantum level of the electronic manifold for simplicity. The encoding transition probability depends on the square of the vibronic transition dipole moment $|\langle g,\mathbf{1}_j|\mu|e,\mathbf{0'}\rangle|^2$. Within the Condon approximation, the vibronic transition dipole moment factors into the electronic transition dipole moment $\mu_{eg} = \langle g|\mu|e\rangle$ and the Franck-Condon factor (FCF) $\langle \mathbf{1}_j|\mathbf{0'}\rangle$, i.e. the vibrational wavefunction overlap integral. We note that the term FCF is alternatively sometimes used to refer to the square of this overlap integral.

The orientation of the vibrational and electronic transition dipole moments, described by the unit vectors $\hat{\mu}_j$ and $\hat{\mu}_{eg}$, respectively, also contribute to the overall transition probability through how they are projected onto the pulse polarization vectors in the laboratory frame and orientationally averaged.[25] Defining the polarization directions of the infrared and visible light fields through the unit vectors $\hat{\varepsilon}_{IR}$ and $\hat{\varepsilon}_{vis}$, the orientational weighting of the excitation probability for a single vibrational mode can be expressed as $Y_{pol}^{(j)} = \langle[\hat{\mu}_j \cdot \hat{\varepsilon}_{IR}]^2[\hat{\mu}_{eg} \cdot \hat{\varepsilon}_{vis}]^2\rangle$, where the subscript $pol = \parallel, \perp$ indicates if the IR and visible fields are set parallel or perpendicular to each other, respectively, or in general denotes their relative angle. $Y_{pol}^{(j)}$depends on the angle between the transition dipole moments, $cos\,\theta_j = (\hat{\mu}_j \cdot \hat{\mu}_{vis})$, according to the following relations: [25], [27]

$$Y_{\parallel} = \frac{1}{15}(2\cos^2\theta_j + 1)$$
$$Y_{\perp} = \frac{1}{15}(2 - \cos^2\theta_j) \tag{1}$$

Taken together, we define the FEIR activity of the $j^{th}$ vibration as the product of these three matrix elements and orientational factor describing the sequential infrared and visible encoding transitions,

$$A_j^{pol} = |\,\mu_j\,|^2 |\,\mu_{eg}\,|^2 |\,\langle \mathbf{1}_j \,|\, \mathbf{0}' \rangle\,|^2\; Y_{pol}^{(j)} \tag{2}$$

In the context of the full response function theory in Ref. 25, this quantity represents the amplitude of the vibration's population pathways in the response function. The FEIR activity defined in this way depends on the choice of pulse polarization but is otherwise independent of all other experimental factors and can be assessed computationally from quantum chemical calculations. For simplicity, we will suppress the superscript $pol$, which unless otherwise noted will be taken to be parallel polarization, and refer to the FEIR activity as $A_j$. The orientational factor $Y_{pol}^{(j)}$ at most modulates the activity by a factor of 3, and is therefore a minor contribution, although we note that all else being equal, parallel transition dipoles ($\theta_j = 0°$ or $180°$) will produce the largest FEIR activities upon optimizing the experimental polarization geometry.

## B. Franck-Condon factors

The FCFs in Eq. (2) can be influenced by several molecular parameters: the displacements of the electronic excited state potential along the vibrational coordinates, the difference in normal mode frequencies in the ground and excited electronic states, and Duschinsky mixing. We investigated the role of these effects by calculating FCFs at three levels of approximation of increasing complexity, all assuming harmonic vibrations. At level I, the FCFs are treated as a function of displacements of electronic state potentials along normal coordinates. At level II, the change in harmonic frequencies between the ground and excited electronic states is added. At level III, Duschinsky mixing is also taken into consideration.

To compute the FCFs, we have taken the approach outlined in refs.28, 29 that utilizes the recursion relations derived by Ruhoff 30 using the formalism of Sharp and Rosenstock,31 and Lermé.32 The $N$ normal mode coordinates in the ground and excited electronic states are related according to the linear transformation

$$\mathbf{Q}_g = \mathbf{J}\mathbf{Q}_e + \mathbf{K}$$

where $\mathbf{Q_g}$ and $\mathbf{Q_e}$ are $N$-dimensional vectors containing the normal coordinates in the ground and excited electronic states. $\mathbf{J}$, the Duschinsky matrix, describes mixing between the ground and excited state normal coordinates, and is an identity matrix for level I and II calculations. $\mathbf{K}$ is a vector of displacements of the electronic excited state potential minimum with respect to the ground state minimum along the normal

coordinates. **K** may be transformed to the dimensionless displacement vector with respect to the ground state coordinates according to $\boldsymbol{\delta} = \mathbf{K}^T \boldsymbol{\Omega}_g^{1/2}$, where $\boldsymbol{\Omega}_g$ is a diagonal matrix of ground state normal mode frequencies.

The dominant contributor to the FCFs is the difference in displacements of vibrations on the ground and excited electronic surfaces. This is the sole consideration under our level I approximation. In this limit the multidimensional overlap integrals factor into products of 1-dimensional FCFs for each normal mode,

$$\langle \mathbf{1}_j \,|\, \mathbf{0}' \rangle_I = \frac{\delta_j}{\sqrt{2}} \langle \mathbf{0} \,|\, \mathbf{0}' \rangle_I . \tag{3}$$

and

$$\langle \mathbf{0} \,|\, \mathbf{0}' \rangle = \prod_{j=1}^{N} \exp\left[ -\frac{1}{2} S_j \right]$$

The latter is the expression for the overlap integral between the zero-quanta vibrational wavefunctions in the ground and excited electronic states. Here $S_j$, the Huang-Rhys factor for mode $j$, are elements of the vector **S**. They are related to the dimensionless displacements, $\delta_j$, by

$$S_j = \frac{1}{2} \delta_j^2 \tag{4}$$

For level II calculations, we also consider vibrational frequency changes between the ground and excited electronic states in addition to the displacements. The FCF is then

$$\langle \mathbf{1}_j \,|\, \mathbf{0}' \rangle_{II} = \frac{\delta_j}{\sqrt{2}} \eta_{j,j'} \langle \mathbf{0} \,|\, \mathbf{0}' \rangle_{II} \tag{5}$$

The 0-0 overlap integral is

$$\langle \mathbf{0} \,|\, \mathbf{0}' \rangle_{II} = \prod_{j=1}^{N} (\zeta_{j,j'} \, \eta_{j,j'})^{1/4} \exp\left[ -\frac{1}{2} S_j \, \eta_{j,j'} \right]$$

where $\eta_{j,j'} = 2\omega_{j'} / (\omega_j + \omega_{j'})$ and $\zeta_{j,j'} = 2\omega_j / (\omega_j + \omega_{j'})$ and $\omega_j$ and $\omega_{j'}$ are the normal mode frequencies in the ground and excited states, respectively.

In level III calculations, the FCF is given as [29]

$$\langle \mathbf{1}_j \,|\, \mathbf{0}' \rangle_{III} = M_j \langle \mathbf{0} \,|\, \mathbf{0}' \rangle_{III} \tag{6}$$

where $M_j$ is the $j^{\text{th}}$ element of vector $\mathbf{M}$ defined as,

$$\mathbf{M} = 2\boldsymbol{\delta}\left(\mathbf{I} - \boldsymbol{\Omega}_g^{1/2}\mathbf{J}\mathbf{X}^{-1}\mathbf{J}^{\dagger}\boldsymbol{\Omega}_g^{1/2}\right)$$

with $\mathbf{X} = \mathbf{J}^{\dagger}\boldsymbol{\Omega}_g\mathbf{J} + \boldsymbol{\Omega}_e$. The 0-0 overlap integral is explained in detail in the supplemantary material.

Note that we when we set $\mathbf{J} = \mathbf{I}$ in the vector $\mathbf{M}$, we get back Eq. (5), and further setting excited state frequencies equal to the ground state frequencies ($\boldsymbol{\Omega}_g = \boldsymbol{\Omega}_e$) takes us back to Eq. (3).

## C. Comparing Computed FEIR Activities with Experiment

### 1. Experimental FEIR brightness and cross-section

To facilitate a quantitative comparison of FEIR activity with experimental measurements for multiple vibrations across multiple molecules with different conditions, we extend the FEIR brightness analysis introduced in Ref. 18. That analysis defined the FEIR brightness of the integrated response of all vibrations within the IR pulse bandwidth by correcting the measured fluorescence intensity for a variety of known experimental factors:

$$q = \frac{F}{rC\eta I_{vis} I_{IR}} \tag{7}$$

where $F$ ($s^{-1}$) is the measured two-pulse FEIR photon count rate at a fixed encoding delay, $I_{IR}$ and $I_{vis}$ are the peak intensities of the IR and visible excitation pulses (GW $cm^{-2}$), $r$ is the pulse repetition rate ($s^{-1}$), $\eta$ is the fluorescence detection efficiency and $C$ is sample concentration ($mol\ L^{-1}$). In analogy to conventional fluorescence brightness, the integrated FEIR brightness can be separated as $q = a\phi$, where $\phi$ is the fluorescence quantum yield and $a$ is the integrated FEIR cross-section ($mol^{-1}\ L\ GW^{-2}\ cm^4$) defined by this relation.

We note that this definition of FEIR cross-section is empirical and practically motivated by the modality of our experiments, and is not given in units fully intrinsic to the molecule. It would be interesting to consider a rigorous connection to the two-photon absorption cross-section (units of Goeppert-Mayer), as was recently done in the case of stimulated Raman scattering.2 The effect of the resonance conditions on the brightness was shown to result in a proportionality with the equilibrium electronic lineshape function

$g(\omega) = \frac{\varepsilon(\omega)}{\int \varepsilon(\omega) d\omega}$ evaluated at the sum of the visible and IR center frequencies $\omega = \omega_{vis} + \omega_{IR}$, where $\varepsilon(\omega)$ is the molar decadic extinction coefficent measured by UV/Vis absorption. The integrated FEIR cross-section corrected for resonance is therefore expressed as $a/g(\omega_{vis} + \omega_{IR})$, and has the units of $mol^{-1}\, L\, GW^{-2}\, cm^3$.

### 2. FEIR activity spectrum and mode-specific cross-sections

We define a molecule's theoretical FEIR activity spectrum

$$A(\omega_{IR}, \omega_{vis}) = \sum_{j=1}^{N} \left|\mu_{eg}\right|^2 \left|\mu_j\right|^2 \left|\langle \mathbf{1}_j \,|\, \mathbf{0}' \rangle\right|^2 Y_{pol}^{(j)} \delta(\omega_{IR} - \omega_j) \delta(\omega_{eg} - \omega_{vis} - \omega_{IR}) \tag{8}$$

as a stick spectrum where each of the $N$ modes has intensity given by its FEIR activity $A_j$. The integrated FEIR cross-section $a$ reflects the response of all the vibrations excited within the bandwidth of the IR pulse spectrum, and in principle the fractional contribution $a_j$ for each vibration may be calculated from its relative peak area in the FEIR spectrum measured at the same encoding delay. Our approach is to connect these mode-specific cross-sections $a_j$ to the theoretical activities $A_j$.

However, this procedure is complicated by the influence of the finite spectra and durations of the excitation pulses as well as vibrational dynamics, most notably multimode coherences, which in many cases produce phase-modulated lineshapes of variable positive or negative sign. Even with measurements taken by the same instrument and experimental conditions, quantitative comparisons of broadband FEIR spectra with DFT calculations for different molecules requires efforts to account for these phenomena. As a first step, we account for the finite IR spectral bandwidth by making the substitution $\left|\mu_j\right|^2 \rightarrow \left|\mu_j\right|^2 I_{IR}(\omega_j)$ in Eq. (8) where $I_{IR}(\omega_j)$ is the normalized IR spectral intensity at the vibrational frequency. As discussed in Ref. 26, this procedure correctly treats the effects of finite pulses on the population response outside the pulse overlap region. We will investigate the success of this simplified analysis with recourse to response function simulations in Sec. IV.

# III. METHODS

## A. Computational methods

## 1. Electronic structure

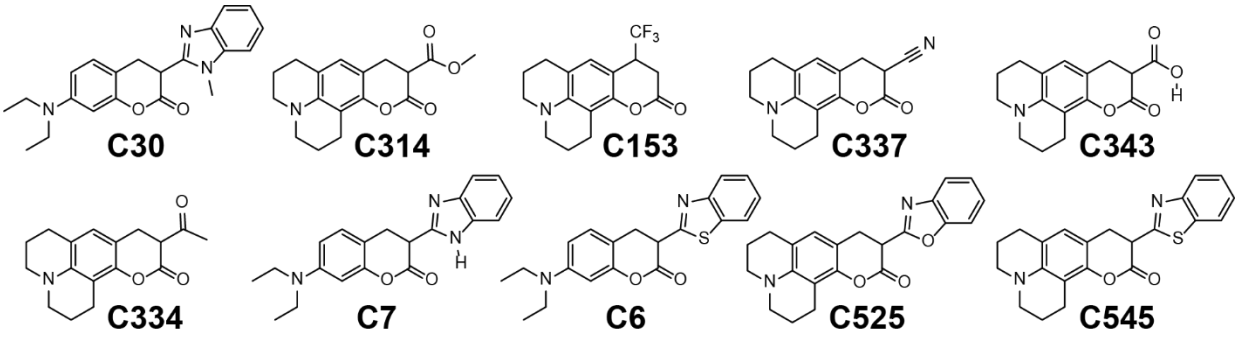


**FIG. 2.** Molecular structures of the coumarin chromophores used in this study.

We investigated ten members of the coumarin family (abbreviated C30, C314, etc.) show in Fig. 2, which were used in the experiments of Ref. 18. Spectroscopic constants and FEIR activities of the molecular vibrations were obtained from electronic structure calculations of the ground and first singlet excited state of the molecule using DFT and time-dependent DFT (TD-DFT), respectively. Gaussian 09 CCP Revision B.0133 was used to optimize the geometry in the electronic ground state and first singlet excited state and perform the corresponding frequency calculations. Calculations for all molecules were performed using the Becke, 3-parameter, Lee–Yang–Parr (B3LYP) hybrid functional34, 35 with 6-31G(d,p) double-zeta basis set with the default convergence criterion (i.e., RMS force threshold set to $3 \times 10^{-4}$) for geometry optimization. For all the structures, the polarizable continuum model (PCM) was used to account for the effect of acetonitrile as the solvent. Frequency calculations were performed at both optimized geometries using the same level of theory to determine the transition energies and transition dipole moments for the normal modes. The vibrational transition dipole moments were computed from the derivatives of the molecular dipole moment along the respective normal mode coordinates. The electronic transition dipole moments were computed from single-point energy calculations of the first excited state by using TD-DFT on the geometry optimized ground state. The relative angles between the vibrational and electronic transition dipole moments obtained from the vectors in the cartesian space were used to calculate the orientational factors $Y_{\parallel}$ and $Y_{\perp}$ according to the equations given in section II C. Existing benchmark studies show that B3LYP demonstrates high levels of accuracy (or minimum % error) for TD-DFT calculations.36 This encouraged us to use B3LYP uniformly for the excited state calculations for all coumarins. Nonetheless, we repeated the calculations for C6 with a long-range corrected functional, ωB97X-D37 and Def2-TZVP basis set, and found that the correlation of the computed IR intensities with the measured molar extinction coefficients for the normal modes worsened (see Sec. S7 of supplementary material).

## 2. Franck-Condon factors

We used the FCclasses code (version 2.1) developed by Santoro co-workers to compute the multidimensional FCFs from the DFT optimized geometries of the ground and excited electronic states. Specifically, we used FCclasses to obtain the dimensionless displacement vectors and Duschinsky matrices and used these to compute FCFs using the expressions for $\langle \mathbf{1}_j \,|\, \mathbf{0'} \rangle$ and $\langle \mathbf{0} \,|\, \mathbf{0'} \rangle$ shown above, using home-written MATLAB scripts.

The dimensionality of the FCFs is dictated by the total number of normal modes of the molecule. Even at the simplest level of approximation (level I) where the FCFs can be written as a product of individual one-dimensional FCFs, the multidimensionality implements itself through the 0-0 overlap integral term. The low frequency modes, typically below 100 $cm^{-1}$ primarily contribute towards the broadening of the electronic lineshape.[38] The 0-0 overlap integrals are strongly affected by large displacements, if any, along the coordinates of these low frequency modes. To exclude the effect of displacements along the normal coordinates of these low-lying modes in our calculations, we have reduced the dimension of the involved matrices to the number of normal modes within the spectral window of our IR pump pulse. For instance, the FCFs of coumarin 6 are 123-dimensional integrals that are computed using a Duschinsky matrix of dimension 123×123, and a 123-dimensional displacement vector. There are 7 normal modes within the IR pump spectral window. Therefore, neglecting the effect of all other normal modes, the FCFs are calculated as 7-dimensional integrals from a truncated 7×7 Duschinsky matrix and a 7-dimensional displacement vector. The influence of dimensionality on the magnitudes of the 0-0 overlap integrals is demonstrated in Section S1.B of the supplementary material.

The computational unit of the FEIR activity $A_j$ can be derived from the units of the vibrational and electronic transition dipole moments. In Gaussian, the vibrational transition dipole derivatives with respect to the normal coordinates, $\mu_j$ are computed in the unit of $\sqrt{km\ mol^{-1}}$ and the electronic transition dipole moments, $\mu_{eg}$ are reported in Bohr-electron or, $ea_0$, where, $a_0$ represents the Bohr radius. These units are related to the conventional units of decadic molar extinction coefficients through linear conversion factors. We report the computed FEIR activities in the units of $km\ mol^{-1}\ e^2\ a_0^2$.

## 3. Finite-pulse response function simulations

Finite-pulse response function simulations of FEIR spectra were carried out as described in Ref. 26. Homogenous-limit expressions for the response function were used with the transition moments and dipole angles taken from the electronic structure calculations. The vibrations were taken to be lifetime-

broadened, and the rates derived from the Lorentzian linewidths of the experimental FTIR spectra. The vibrational coherence dephasing between all pairs of modes a were taken as 400 fs, and the electronic and vibronic dephasing times were set to 10 fs. The IR and visible pulses were given Gaussian spectra chosen to match the experimental pulse characteristics. The IR pulse had frequency $\omega_{IR} = 1620\,\text{cm}^{-1}$, FWHM $\Delta\omega_{IR} = 140\,\text{cm}^{-1}$, and second order dispersion coefficient of $-7800\,\text{fs}^2$ to produce a chirped duration of 230 fs. The visible pulse was taken to be transform-limited with $\omega_{vis} = 19360\ \text{cm}^{-1}$ and $\Delta\omega_{vis} = 46.7\ \text{cm}^{-1}$, producing a duration of 315 fs.

## B. Experimental

Our analysis makes use of the data previously reported in Ref. 18, and the detailed experimental methods and materials used can be found therein. For convenience, we summarize the key features below.

**Preparation of solutions**: Stock solutions were prepared by weighing out the required masses of solid dyes in clear glass vials and dissolving in acetonitrile ($CH_3CN$) or methanol ($CH_3OH$). Sample solutions for UV/Vis, fluorescence, FTIR and FEIR measurements were prepared by pipetting out the required volumes of stock solutions in clear glass vials, drying out the solvent by passing $N_2$ and dissolving the solid residue in either acetonitrile (for UV/Vis and fluorescence measurements) or deuterated acetonitrile ($CD_3CN$) (for FTIR and FEIR measurements).

**UV/vis and fluorescence measurements:** The UV/vis spectra were acquired from 40 μM on an Agilent Cary 5000 UMA dual-beam spectrophotometer. The fluorescence excitation/emission surfaces were acquired from 2-5 μM solutions on a Horiba Fluorolog-3 spectrofluorometer. The samples were ensured to have an absorbance of less than 5% to avoid errors in the fluorescence measurements arising from inner filter effect.

**FTIR measurements:** Dye samples of 2-10 mM concentrations were used to measure the FTIR spectra on a Bruker Tensor 27 FTIR spectrometer. The sample cell was prepared by enclosing ~60 μL of sample solution between two $CaF_2$ windows with path length maintained between 50-500 μm using Teflon spacers. The measured absorption spectra are converted to the units of molar extinction coefficient according to Beer's Law.

**FEIR measurements:** FEIR spectra were acquired on 30 – 100 μM solutions using the instrument and methods described previously.17, 18, 26 The mid-IR excitation pulses were centered between 1600 – 1620 $\text{cm}^{-1}$, had a FWHM bandwidth of ~ 140 $\text{cm}^{-1}$, and a pulse duration of 230 fs. The visible excitation pulses

were centered at 516.5 nm, with a bandwidth < 2 nm and a pulse length of ~315 fs. For acquiring Fourier transform FEIR spectra, the IR pulses were sent through a Mach-Zehnder interferometer to generate collinear IR pulse pairs with the delay controlled by a nanopositioning stage, and an identical stage is used to set the IR-visible encoding delay $\tau_{enc}$. The relative polarization between the IR and visible pulses was set by controlling the visible polarization by a half waveplate. The IR and the visible pulses focused at the sample position by a ZnSe asphere and a 0.8NA Zeiss objective, respectively. The fluorescence signal was collected with the same objective, passed through a long-pass dichroic optic and focused onto the ~50 μm active area of an avalanche photodiode.

# IV. RESULTS AND DISCUSSION

## A. FEIR activity analysis of C6 normal modes

### 1. DFT calculations of normal mode frequencies in the ground state

To illustrate the computations and analysis performed for all molecules, we begin with detailed results for Coumarin 6 (C6), the FEIR chromophore with the best combination of brightness and contrast measured to this time.[17, 18] FIG 3 compares the measured FTIR absorption spectrum of C6 in the frequency region 1450 – 1800 $cm^{-1}$ with the stick spectrum obtained from DFT normal mode calculations on the optimized ground state. Five distinct vibrational resonances are observed in the experimental spectrum: Four ring stretch modes with frequencies at 1484, 1515, 1586, and 1616 $cm^{-1}$, and the lactone carbonyl stretch mode at 1712 $cm^{-1}$, which we denote as R4, R3, R2, R1, and C=O respectively. Computed normal mode frequencies for C6 lie within ±10 $cm^{-1}$ of experimental values when a scaling factor of 0.973 is applied (See section IV B.1), which is close to the empirical scaling factor of 0.96 for B3LYP/6-31G(d,p) level of calculation.[39] FIG 4 shows snapshots of the computed atomic displacement vectors, and the transition dipole moment vectors for these normal modes. The skeletal ring vibrations marked R1, R2, and R3 are the dominant contributors towards the FEIR activity of the molecule.[18] R4 is not sufficiently excited by our IR pump pulse to gauge its FEIR activity in our analysis.

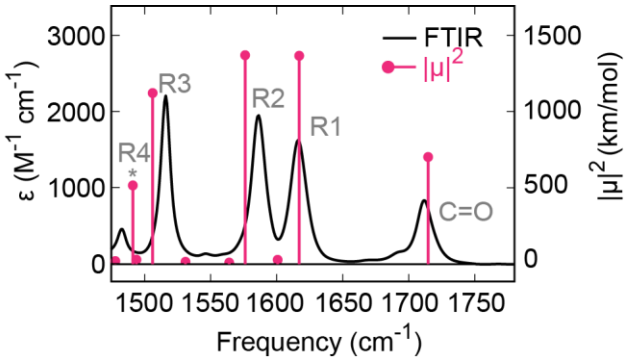


**FIG 3**. FTIR absorption spectrum of C6 in deuterated acetonitrile compared with the DFT normal mode calculations on the ground state in the spectral region of 1450 – 1800 $cm^{-1}$. Experimental spectrum is shown in black (left y axis), and calculated DFT spectrum is shown in magenta (right y axis). The experimental peaks at 1484, 1515, 1586, 1616 and 1712 $cm^{-1}$ are denoted as R4, R3, R2, R1 and C=O respectively. The * indicates that mode R4 lies beyond the IR-pumped spectral region, and is not observed in our FEIR experiments. The DFT frequencies are scaled by a factor of 0.973.

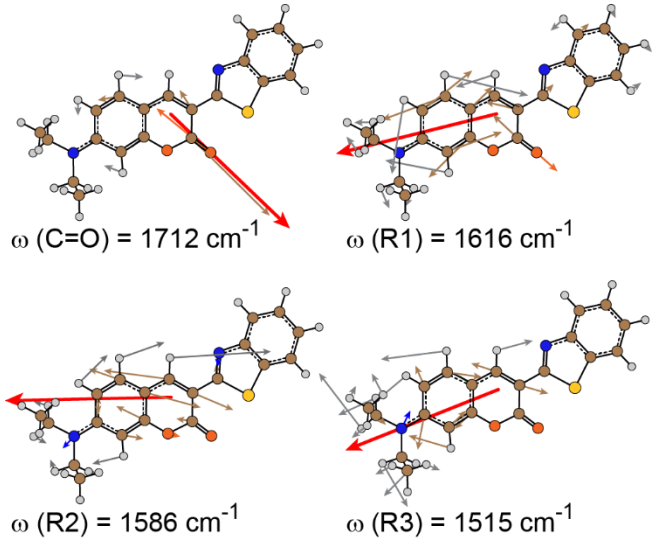


**FIG 4**. Snapshots of the DFT-calculated normal mode displacement vectors for R3, R2, R1 and C=O. Grey arrows indicate atomic displacements, color-coded elementwise (H=grey, C=brown, N=blue, O=orange, S=yellow), scaled relative to the maximum displacement. The transition dipole moment vectors are indicated by red arrows (magnitudes scaled for visualization). The experimental frequencies from the assignment are indicated.

## 2. FEIR selection rules

To gain insight into "FEIR selection rules", i.e. if and to what extent a vibration appears bright, we compare the FEIR and FTIR spectra. Figure 5 shows the FEIR spectrum of C6 at $\tau_{enc} = 600$ fs with the pulse spectrum used in the measurement overlaid. This encoding delay represents a region outside of pulse overlap, and exhibits peaks in the FEIR spectrum that are essentially absorptive, which allows for straightforward comparison with the FTIR spectrum. However, as discussed in Ref. 26, there is still a non-

negligible coherence contribution, which we will address in Sec. IV A 4. In measurements on some of the other coumarins studied, coherence contributions at early encoding delays more strongly apparent, as discussed in Section IV B.

Since the intensity of peaks in the FEIR spectrum is spectrally filtered by the IR pulse bandwidth, we scale the FTIR by the same pulse spectrum for comparison. The peak frequencies and lineshapes are the same in both spectra, as expected for ground -state vibrational spectroscopy. However, the difference in the relative intensities of the resonances between FEIR and FTIR spectra indicate the different selection rules for these methods. While both methods require IR activity, FEIR also requires sufficiently large FCFs for the fluorescence encoding transition. Evidently, the R1, R3 and lactone C=O stretch modes are suppressed in FEIR activity relative to the intense R2 ring mode. This is qualitatively well-reproduced by the FEIR activity spectrum, calculated using Eq. (8)**Error! Reference source not found.** in the computational units of $km\ mol^{-1}\ e^2\ a_0^2$.

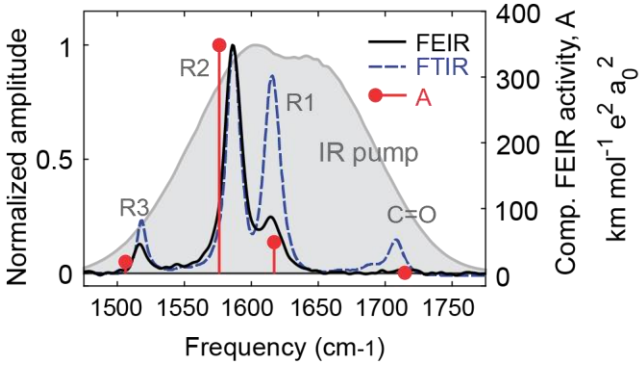


**FIG 5.** Comparison of the FEIR spectrum, FTIR spectrum and computed FEIR activities of C6. FEIR spectrum (solid black) with the FTIR spectrum (dashed navy) scaled by the IR pump spectrum (grey shaded area) showing the suppression of R3, R1, and C=O relative to R2. The FEIR spectrum was acquired under the parallel polarization scheme at $\tau_{enc} = 600$ fs, and normalized to the intensity of R2 (left y axis). The FEIR activity stick spectrum calculated using Eq. (8) is shown in red (right y axis).

As evident from Eq. (8)**Error! Reference source not found.**, the product of the squares of FCF and the vibrational transition dipole shapes the FEIR activity for a normal mode. In the simplest approximation, FCFs are solely dependent on the Huang-Rhys factors, $S$. Furthermore, for $S \leq 0.1$ that applies for the normal modes we studied, $S \approx FCF^2$ (see Sec. S2 of supplementary material). Fig. 6a shows a scatter plot of the squares of the vibrational transition dipoles $|\mu_j|^2$ against the Huang-Rhys factor for all normal modes of C6. There is little correlation between these variables for different modes, but we see that the four prominent FEIR active normal modes in Fig. 5, all lie in the top right quadrant of the correlation

plot in the region bounded by $S|\mu|^2$ >10 km/mol (marked by a dashed purple line). This indicates that there is a small number out of the 123 modes that dominate the FEIR activity of the molecule.

The stringent requirements for FEIR activity become clearer in Fig. 6b which shows the plot of the product of the two quantities $S|\mu|^2$ against the calculated frequencies. The plot identifies only 5 out of 123 normal modes that have a non-negligible $S|\mu|^2$ (>10 km/mol), of which 3 are shown in FIG 4, along with C=O whose $S|\mu|^2$ value falls below the threshold of 10 km/mol. The other vibrations marked by (*) are the previously identified ring mode R4, and another ring stretching mode at 1387 $cm^{-1}$ observed in the FTIR spectrum at 1358 $cm^{-1}$, and lie outside the IR pump spectral window (atomic displacements in Fig. S3.8). These results indicate that only the molecule's ring skeletal stretching modes are strongly FEIR active, whereas C-H ring stretching modes, high frequency C-H stretching and bending modes of the diethylamine and benzothiazole substituents (> 3000 $cm^{-1}$), and low frequency modes <1300 $cm^{-1}$ do not contribute. It is interesting to consider these results in the context of the observations initially made by Kaiser and co-workers in their original work,[5] where they concluded that the response from C6 excited with IR pulses centered at 3200 $cm^{-1}$ originated from C-H stretches, but, upon further in-depth studies, [7] deduced that the origin of the response was instead due to combination bands involving the ring stretches in the 1600 $cm^{-1}$ region.

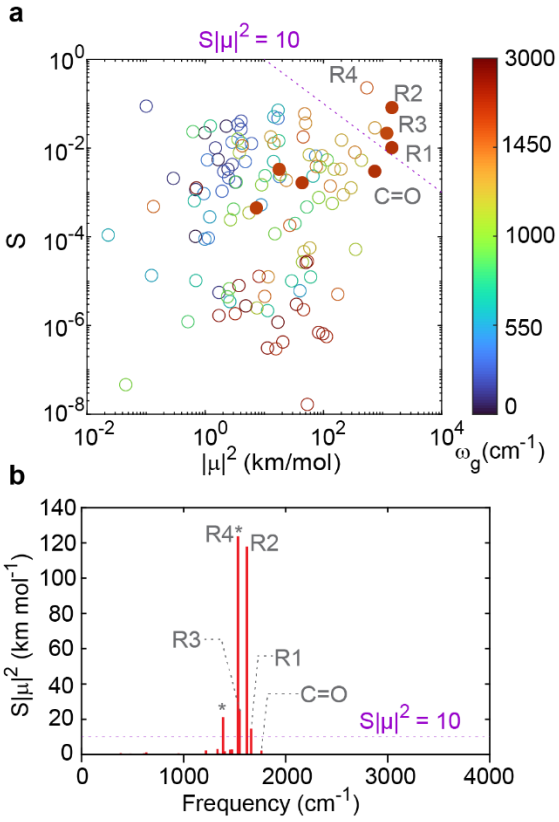


**FIG. 6.** Demonstration of FEIR selection rule. (a) Correlation between the infrared intensities $|\mu_j|^2$ and Huang-Rhys factors $S_j$ for the 123 normal modes of C6 (circles). The color indicates its vibrational transition frequency (see color bar). The solid circles indicate the modes lying within the spectral window of the IR pump pulse. The detection threshold for our experimental studies, $S|\mu_j|^2 = 10$ is indicated with a dashed purple line. (b) The $S|\mu|^2$ product as a function of frequency for all normal modes of C6, demonstrating only 5 out of 123 modes have non-negligible contribution to the overall FEIR activity of C6. (*) indicates the modes lie outside our experimental window but are predicted to have large FEIR activity.

To look at the effect of frequency changes between ground and excited electronic states and Duschinsky mixing on the FCFs, we employ Eqs. (5) and (6) to calculate the FCFs at approximation levels II and III respectively. Comparing the values of FCFs under these approximations for R3, R2, R1 and C=O vibrations for C6 (Table 1), we observe essentially no change (<1%), indicating that the Huang-Rhys factor is sufficient to determine the magnitude of these integrals, while mode mixing and frequency changes play a negligible role. This is also in agreement with the calculated FCFs of C6 modes reported by Burghardt and co-workers.[29] This observation extends to all the coumarins investigated in this paper, and allows us to use the intuitive displaced harmonic oscillator model to understand FEIR activity.

**Table I.** Experimental and calculated frequencies (scaled) of the three FEIR active vibrational modes of C6, in addition to the lactone carbonyl, their extinction coefficients $\varepsilon$ (integrated over the band), calculated transition dipole moments $\mu$, magnitudes of Franck-Condon factors at three levels of approximation, relative angles between vibrational and electronic transition dipole

moments from electronic structure and normal mode calculations $\theta$, and the calculated and measured anisotropy values. Experimental anisotropies are obtained from the average value across the FWHM of individual peaks.

| Mode | $\omega_j$ ($cm^{-1}$) | | $\varepsilon/10^3$ ($M^{-1}\,cm^{-2}$) | $\lvert\mu\rvert^2/10^3$ (km/mol) | Franck-Condon Factor $\langle \mathbf{1}_j \mid \mathbf{0'} \rangle$ | | | $\theta_j$ (°) | Anisotropy, $r$ | |
|---|---|---|---|---|---|---|---|---|---|---|
| | expt. | calc. | | | I | II | III | | calc. | expt. |
| R3 | 1515 | 1506 | 31.09 | 1.18 | 0.137 | 0.136 | 0.137 | 3.2 | 0.40 | 0.26 |
| R2 | 1586 | 1576 | 36.07 | 1.44 | 0.268 | 0.264 | 0.266 | 19.1 | 0.33 | 0.28 |
| R1 | 1616 | 1617 | 32.63 | 1.43 | -0.094 | -0.094 | -0.094 | 6.7 | 0.39 | 0.35 |
| C=O | 1712 | 1714 | 18.86 | 0.74 | -0.051 | -0.051 | -0.051 | 116.0 | -0.08 | -0.05 |

## 3. Vibrational and electronic transition dipole orientation and anisotropy

As discussed in Sec. II A, the orientational factor for a vibration's population response can be calculated from the computed angle ($\theta_j$) between the vibrational and electronic transition dipoles using Eq. (1)**Error! Reference source not found.**, and result in a polarization anisotropy value of

$$r_{calc} = \frac{1}{5}(3\cos^2\theta_j - 1). \tag{9}$$

We note that this relation only holds when we neglect the contribution from coherence pathways. To further assess the accuracy of the electronic structure calculations, we compare the anisotropies calculated from the computed angles with experimental FEIR anisotropies. Fig. 7a shows the transition dipole vectors computed for the R3, R2, R1, and C=O modes and the electronic transition. Experimental anisotropies were determined from the parallel and perpendicular polarization FEIR spectra, $S(\omega)$, using

$$r_{\text{expt}} = \frac{S_{\parallel} - S_{\perp}}{S_{\parallel} + 2S_{\perp}}. \tag{10}$$

Experimental measurements of the parallel and perpendicular FEIR spectra and the corresponding anisotropies are presented in Fig. 7b and reported in Table I. The reported values are averages over the corresponding linewidths. The FTIR spectrum is shown on the top panel for reference. R1, R2 and R3 have anisotropy values close to that expected for parallel or anti-parallel dipoles ($r = 0.4$), while the lactone C=O mode has an anisotropy close to zero, as expected for vibrational dipoles oriented close to the magic angle with the electronic transition dipole moment ($\theta_j \approx 54.7°$ or $125.3°$). The errors associated with the measurements lie within 2 – 15%, the minimum being for R1 and maximum for R3. The anisotropy of the

C=O mode, shown as a separate panel was determined from a separate experiment with the IR pump pulse tuned to ~1720 $cm^{-1}$. The full comparison of the calculated and measured anisotropies of the normal modes of all ten coumarins is discussed in Sec. IV. B.2.

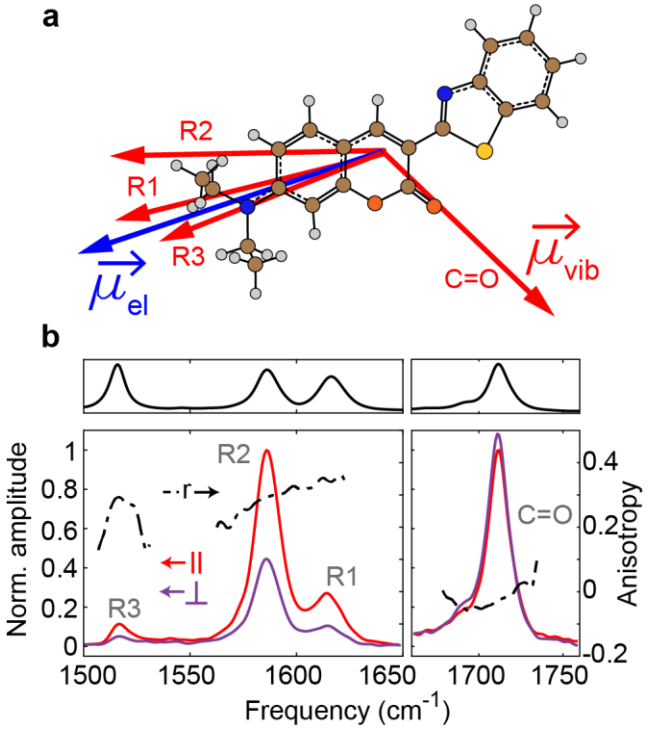


**FIG. 7.** Relative orientations of transition dipoles and polarization anisotropy. (a) Ground-state optimized geometry of C6 with the electronic (blue arrow) and vibrational (red arrows) transition dipoles for R3, R2, R1, and C=O. (b) Polarization-dependent FEIR spectra and anisotropy of normal modes calculated using Eq. (10)

## 4. Effects of vibrational coherence and finite pulses on FEIR spectra

As ultrafast nonlinear measurements, FEIR spectra with broadband pulses are influenced by ground state vibrational dynamics initiated by the IR excitation fields, which can complicate the comparison against static parameters derived from electronic structure calculations. Vibrational coherences excited by the short IR pulses give rise to beats and phase distortions in FEIR spectra during $\tau_{enc}$, and finite pulse effects can introduce additional complexities, especially at early $\tau_{enc}$. Consequently, both population and coherence pathways simultaneously influence the overall FEIR activity that cause deviations from, or even change the signs of the activities predicted using Eq. (8). As shown recently,[25, 26] response function simulations capture these phenomena and produce insight into the detailed shape and $\tau_{enc}$ evolution of spectra. To

discuss how these effects can be accounted for within our current analysis, we reproduce a part of the results from Ref. 26 in this section.

Figure 8(a) shows the experimental FEIR spectrum of C6 as a function of encoding delay. The spectral intensities are observed to rise over several hundred femtoseconds before damping on picosecond timescales, and the R3 mode is particularly strongly modulated by coherent beats. Furthermore, negative contributions are observed at early waiting times. The $\tau_{enc}$-dependent FEIR spectrum simulated with DFT-computed parameters is shown in Fig. 8(b). As input, we used the vibrational transition dipole moments, frequencies, FCFs and orientational factors. We observe excellent qualitative agreement between the experimental and simulated spectral response. Beating amplitudes and peak growth and relaxation times are effectively simulated, as are the negative contributions to the signal for delays <500 fs. The latter were shown to originate from coherences involving two FCFs and/or transition dipole projections that were of opposite sign. One significant difference is an apparent $\tau_{enc}$ offset of ~100 fs in the shape of the spectral response of the experiment relative to simulations, as highlighted by the dashed lines. The origin of this offset remains unclear, but is on the order of the experimental uncertainty in determining the true zero point of the $\tau_{enc}$ delay.26 We therefore consider the experimental spectra at encoding delays 600 fs and 100 fs for the purpose of comparing with simulations at encoding delays 500 fs and 0 fs respectively.

Other errors are present due to inaccuracies in the DFT calculations, e.g. in the calculated vibrational frequencies and transition dipole moments. To extract these ground-state vibrational parameters from experiment, the FTIR spectrum was fit to a sum of Lorentzian functions, and the frequency and vibrational transition dipole values were extracted from the fit parameters (Sec. S4). Exchanging the calculated with experimentally determined frequencies and vibrational transition moments produces the simulated spectrum in Fig. 8(c), which shows even closer agreement to the experiment.

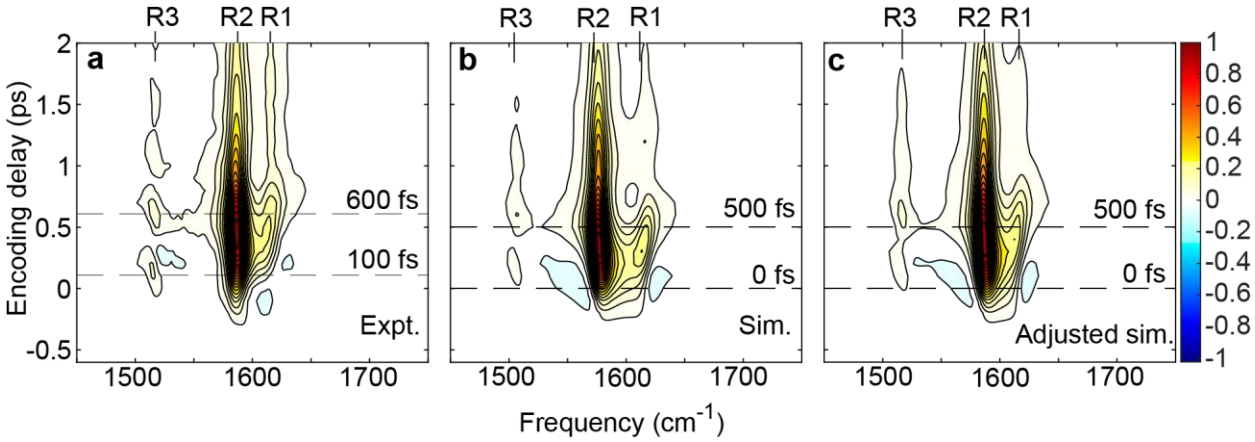

**FIG 8.** Qualitative comparison of FEIR intensities and computed FEIR intensities of C6 normal modes. FEIR spectra as a function of encoding delay, experimental (a) , simulated with all parameters from DFT (b), and simulated with vibrational transition dipoles and frequencies adjusted from FTIR (c). Dashed black lines correspond to the slices shown in Fig. 9.

Despite their accuracy, the computational complexity of these response function simulations adds a barrier to implementing them in high-throughput situations, and the outcome is specific to the pulse characteristics in the experiment. To test a simple indicator of the effective coherence-influenced FEIR activity of individual normal modes under broadband excitation, we use a modified version of Eq. (2)

$$I_j = \sum_i \left|\mu_{eg}\right|^2 \mu_i \mu_j \langle \mathbf{1}_i | 0' \rangle \langle 0' | \mathbf{1}_j \rangle \, Y_{pol}^{(i,j)}. \tag{11}$$

Here, $i$ sums over the $N$ molecular vibrations, with $i = j$ giving the population pathway and $i \neq j$ representing all coherence pathways involving different pairs of normal modes. The signs of these coherence cross-terms be either positive or negative, depending on the relative signs of the FCFs and the orientational factors, $Y^{(i,j)}$. The latter are now determined by the orientation of two vibrational transition dipoles ($\hat{\mu}_i$ and $\hat{\mu}_j$) relative to the electronic transition dipole orientation ($\hat{\mu}_{eg}$). For the case of co-planar transition dipole moments relevant to our experiments on coumarins, these expressions are[26]

$$\begin{aligned} Y_{\parallel}^{(i,j)} &= \frac{1}{15}\left(2\cos(\theta_i - \theta_j) + \cos(\theta_i + \theta_j)\right) \\ Y_{\perp}^{(i,j)} &= \frac{1}{30}\left(3\cos(\theta_i - \theta_j) - \cos(\theta_i + \theta_j)\right) \end{aligned} \tag{12}$$

Importantly, we note that the static coherence-influenced activities $I_j$ in Eq. (11) are only relevant to FEIR spectra near $\tau_{enc} = 0$, because the coherences acquire phase as $\tau_{enc}$ evolves and oscillate at the respective frequency differences between modes. For comparison to experiments, we weight the individual IR transition moments again by the spectral intensity of the IR light at the resonance frequency using a replacement similar to before in Sec II C 2: $\mu_i \mu_j \rightarrow \mu_i \mu_j \sqrt{I_{IR}(\omega_i) I_{IR}(\omega_j)}$.

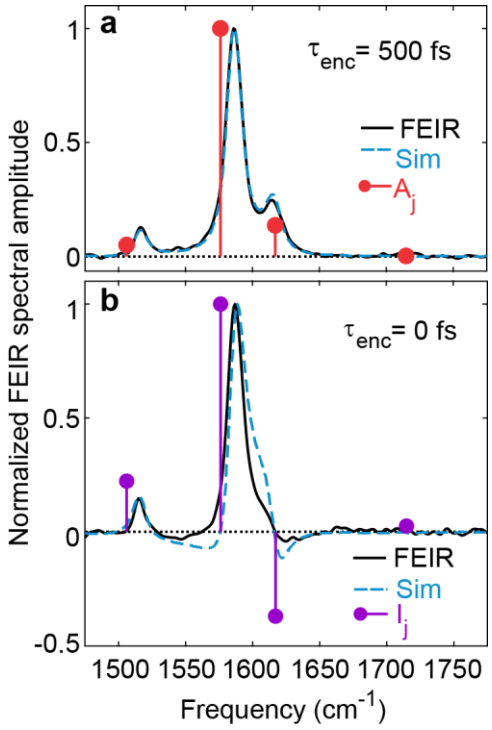


**FIG 9.** (a) Comparison of experimental and simulated spectra at different encoding delays. (a) Comparison of the experimental spectrum at $\tau_{enc} = 600$ fs (black) with the simulated spectrum at $\tau_{enc} = 500$ fs (blue), overlayed by the FEIR activity spectrum (stick spectrum), derived from Eq. (8). (b) Comparison of the early-time FEIR spectra, $\tau_{enc} = 100$ fs for experimental (black) and $\tau_{enc} = 0$ for simulated spectra (blue), overlayed by the effective coherence-influenced FEIR activity under broadband excitation, derived from Eq. (11) (stick spectrum).

Figure 9(a) shows a comparison between the experimental spectrum at $\tau_{enc} = 600$ fs and the simulated spectrum at $500$ fs, where the peaks are absorptive. Comparing the simulated and experimental spectra shows that the peak intensity pattern is identically reproduced by our simulation, and also qualitatively matches the FEIR activities predicted by Eq. (8), which do not account for coherence. This fortuitous situation was shown to result in part from the particular alignment of coherence phase evolution due to the frequency differences between the modes and their relative FCF signs.[26] The underestimation of the R1 and R3 intensities at this encoding delay by the DFT-calculated FEIR activities is likely due these coherences.

In Fig. 9(b), we look at the spectra at $\tau_{enc} = 0$ fs (100 fs for experiment), which falls in the region most heavily affected by coherences. The response from R1 is significantly influenced by its coherence with R2. Given their FCFs have opposite signs (Table I), the coherence pathways should have a negative contribution to the overall FEIR response. The FEIR amplitude of R1 indeed has a negative amplitude in

the experimental spectrum and is correctly reproduced in the simulation. The coherence-influenced FEIR activity (Eq. (11))**Error! Reference source not found.** also predicts the sign of R1 correctly, but is not able to capture the relative amplitudes well. However, when we invoke the simulation based on response function, and add in the finite pulse effects with the pulse characteristics taken from the experiment, the simulated spectrum predicts the relative intensities and signs with good qualitative agreement. To summarize, our comparisons suggest that while the DFT calculations yield accurate results for the molecular factors—importantly including the signs of the FCFs and orientational factors—dynamic multimode coherences and pulse convolution significantly modulate the amplitudes of the broadband FEIR response at early encoding delays, complicating static predictions based on matrix elements alone.

## B. Assessing computational predictions across the coumarin family

### 1. Transition strengths and frequencies

We begin our investigating of the accuracy of computed FEIR activities by analyzing the vibrational and electronic transition frequencies and intensities. The comparison between experiment and DFT calculations illustrated above with C6 are for the most part representative across the coumarin family. Fig. 10 presents the comparison of the vibrational frequencies and computed IR intensities, electronic oscillator strengths and $S_0 \rightarrow S_1$ transition frequencies across members of the coumarin family. The harmonic computed frequencies across all molecules are highly correlated with experimental frequencies, related by a scaling factor of 0.973 (Fig. 10a). The squares of the vibrational transition dipole moments show a reasonable linear correlation with experimental integrated molar extinction coefficients (Fig. 10b), and the error associated with the calculations of these absolute amplitudes directly carries into the prediction of FEIR activities. The experimental electronic oscillator strengths (determined previously in Ref. 18) are also highly correlated with computed oscillator strengths for HOMO-LUMO transitions across all molecules, related by a scaling factor of 0.69 (Fig. 10c). The experimental $S_0 \rightarrow S_1$ transition frequencies $\omega_{vis}$(expt), derived from the absorption maxima in the UV/Vis spectra18 also show a strong linear correlation with the corresponding TD-DFT calculated transition frequencies ($\omega_{eg}$), related by a scaling factor of 0.942 (Fig. 10d), with C314, C337, C343 and C334 treated as outliers. The relatively poor correlation of the electronic transition energies can be attributed to the errors in TD-DFT calculations, which are typically about 0.3-0.4 eV40. For molecules like the coumarins that involve bond length alteration and quinoidization as a result of conjugation, such errors have been reported previously.24, 36,

41, 42 The computed FCFs at Level I for vibrations >1000 $cm^{-1}$ lie within 2% of the Level II and Level III values (Fig. S1.1).

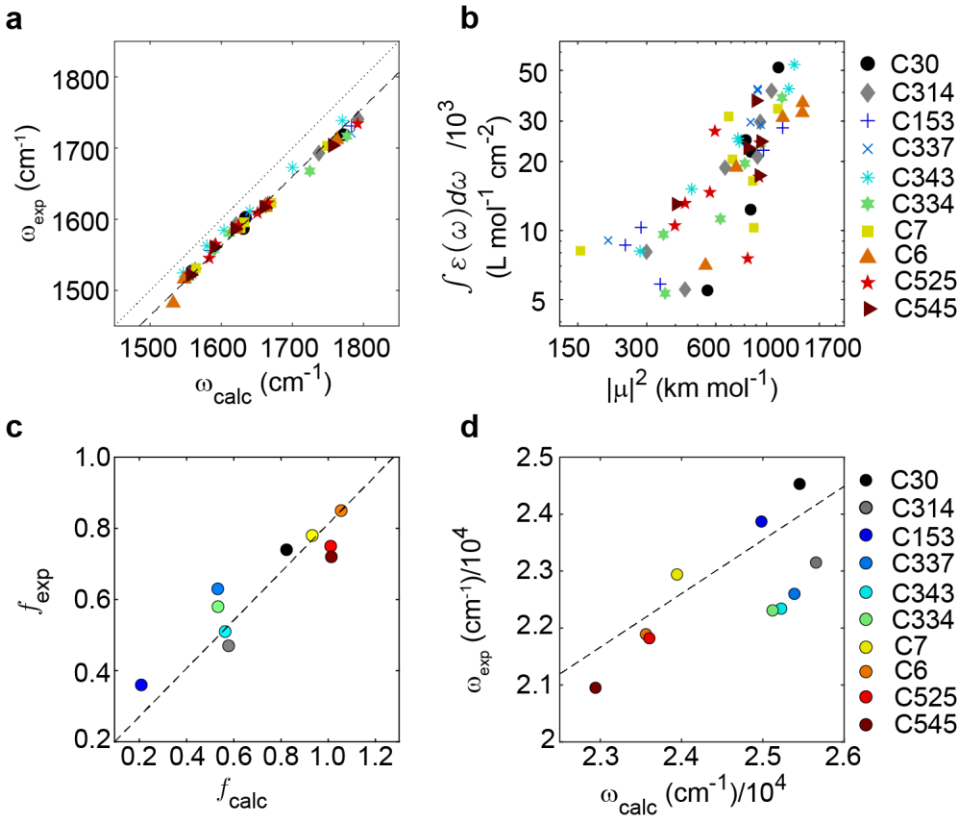


**FIG 10.** Comparison of experimental IR and electronic spectroscopy with computed values. (a) Correlation between the experimental and calculated IR vibrational frequencies. The correlation is fit to a linear function and yields a slope of 0.973, shown by the black dashed line. The grey dash-dot line, denoting $\omega_{exp} = \omega_{calc}$ is added for reference. (b) Correlation between the experimental IR molar extinction coefficients and corresponding calculated IR intensities for the normal modes of coumarins in the frequency range of 1450 – 1800 $cm^{-1}$. (c) Correlation between TDDFT-calculated and experimental oscillator strengths for the $S_0 \rightarrow S_1$ transition, with a linear fit showing $f_{exp} = 0.69 f_{calc}$ (d) Correlation between TDDFT-calculated $S_0 \rightarrow S_1$ transition frequencies and the corresponding experimental A linear fit (dashed black line) establishes a relationship of $\omega_{exp} = 0.942\ \omega_{calc}$.

## 2. Dipole orientation

The methods described in detail above for C6 (Fig. 7) were also applied to all the molecules within the coumarin family shown in Fig. 2. The polarization-dependent FEIR spectra from which the anisotropies were deduced are shown in Sec. S6 of the supplementary material. As in the case of C6, the anisotropy values are taken as average across the corresponding linewidth of the vibrational peaks. The relationship between the calculated and experimental anisotropies for all FEIR active normal modes is shown in Fig. 11. One observes an overall linear correlation, highlighting the accuracy to which the DFT calculations

predict the relative orientation of the vibrational and electronic transition dipole moments. We note that the uncertainty associated with each experimental data point reflects the frequency-dependent variation of the measured anisotropy within the resonance, and therefore will not necessarily be improved by further signal averaging. The origin of this variation is unclear, but is likely dominated by the contribution of coherence pathways, as well as being influenced by the partial overlap of resonances and small experimental phase errors in acquiring the Fourier transform spectra.

Overall, the ring mode transition dipoles (highlighted within the grey box) exhibit a near-parallel orientation with the electronic transition dipole, resulting in anisotropy values close to the theoretical maximum of 0.4. While the DFT results predict anisotropies for these modes in the range of 0.3-0.4, the corresponding experimental values are consistently slightly lower. One possible explanation for this discrepancy is the effect of impure linear polarization in the experiments.[26]

The carbonyl modes show consistency between the calculated and measured anisotropies, which lie in the range of –0.2 - 0.2. As the lactone carbonyls of many of these coumarins have negligible FEIR activity, their corresponding anisotropy measurements are accompanied by significantly larger uncertainties. However, C153, C337, and C343, exhibit large lactone carbonyl FEIR activities and their anisotropies are measured with much better accuracy. Similarly, the anisotropy for the lactone carbonyl of C6 was determined by tuning the IR pulse to 1720 $cm^{-1}$, directly pumping the mode. The correlation is particularly good for these data points.

The coumarins C314, C343, and C334 have two different carbonyls: a lactone carbonyl as a part of the coumarin core, and a carbonyl as a functional group (-$COOC_2H_5$, -COOH, and -$COCH_3$ respectively). The two carbonyl transition dipoles are oriented differently in the molecular frame, and are experimentally distinguished through their different anisotropy values. While the lactone carbonyls generally have an anisotropy close to zero, indicating that it is oriented at close to the magic angle (54.7°) with the electronic transition dipole, the carbonyl in the functional group typically exhibits a value in the range of –0.1 to –0.2. This distinction proves useful in assigning spectra. For instance, in most cases the lactone carbonyl peak appears >1700 $cm^{-1}$, with the carbonyl on the substituent appearing at lower frequency <1700 $cm^{-1}$. However, for C343 the DFT calculation indicates the formation of an intramolecular hydrogen bond between the -COOH group and the lactone carbonyl, causing the latter to redshift and reversing their frequency ordering (see normal mode snapshots in Fig. S3.5 of the supplementary material). Indeed, this assignment is supported by the FEIR anisotropy of these two modes.[26] Overall, this good agreement against

experimental FEIR anisotropy indicates the DFT calculations accurately predict the vibrational and electronic transition dipole orientations.

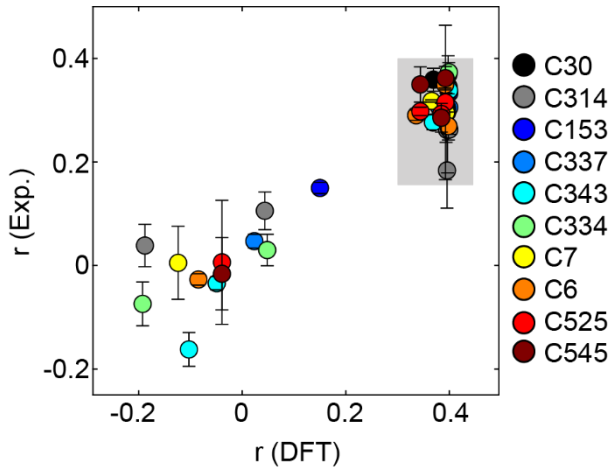


**FIG 11.** Correlation between calculated and experimental anisotropies for normal modes of ten coumarin dyes (see Sec. S6. The error bars represent the standard deviation in the experimental anisotropy due to variation across each band's lineshape.

## 3. Integrated FEIR cross-section

In our calculations across the coumarins, typically 3-8 normal modes exhibit significant FEIR activity with $S|\mu|^2$ >10 km mol$^{-1}$. These modes are typically delocalized ring modes involving C=C stretches conjugated with C-H bends. Notable exceptions include the lactone carbonyl stretches of C153 and C337, which exhibit large $S|\mu|^2$ values of 128 and 26 km mol$^{-1}$ respectively (see Table SI in Supplementary Material). In most cases, these modes are also those excited within the bandwidth of the IR pulses in our measurements.

To assess the ability of the calculations to predict overall FEIR brightness, we target the experimental FEIR cross-section $a$ (Eq. (7))**Error! Reference source not found.**, scaled by the electronic lineshape factor $g(\omega_{vis} + \omega_{IR})$. This quantity, $a/g(\omega_{vis} + \omega_{IR})$, reflects the response of all vibrations excited within the IR pulse spectrum corrected for the variable electronic resonance conditions across measurements. As a comparable quantity from calculation we use the sum of the computed activities $A = \sum_j A_j$, with the $A_j$ from Eq. (8) corrected for IR pulse spectrum as in Sec. II C 2. Figure 12 shows the relationship between these two quantities across the series of ten coumarins, which exhibit a linear correlation with Pearson's correlation coefficient ( $\rho$ ) of 0.7.

This degree of correlation, while subject to non-negligible dispersion, indicates that the calculated activities can predict the strength of the FEIR response at the order of magnitude level or better. Indeed, we note the roughly tenfold spread in the resonance-corrected FEIR cross-sections across the coumarin series, even though overall they possess similar vibrational extinction coefficients, electronic oscillator strengths, and fluorescence quantum yields. This variation underscores the concerted influence of all the molecular factors, and particularly vibronic couplings, which are among the most difficult quantities to access with conventional spectroscopic characterization methods. The calculations predict substantial FEIR activities for C6, C7, C30, and C525. Within the limited resonance conditions accessible by the fixed visible encoding frequency of our current experimental setup, we have validated these predictions for C6 and C7, confirming their SM sensitivity as demonstrated in Ref. 18.

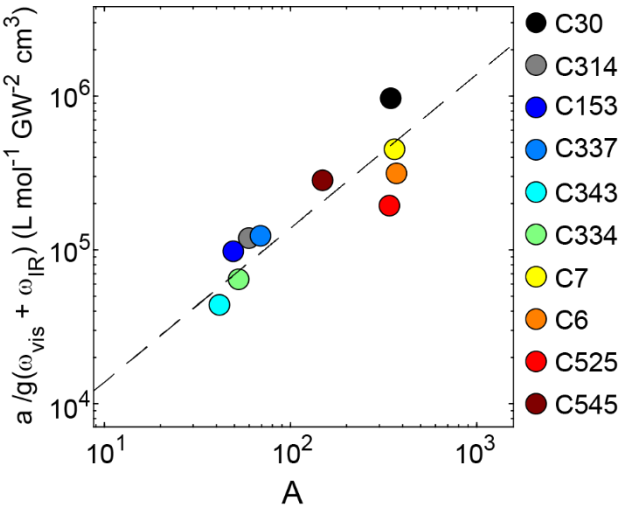


**FIG 12**. Correlation between the sum of computed FEIR activities of normal modes lying within the IR pump spectral window (A) and the lineshape-normalized experimental total FEIR cross-sections of molecules across the coumarin series (experimental data from Ref. 18).

The dispersion observed in the correlation likely has contributions from our simplified static analysis of FEIR activity that neglects the effects of population relaxation, vibrational coherence, and finite-pulse durations. These factors collectively make the quantitative comparison of mode-specific FEIR activities with the experimental peak intensities in broadband spectra more challenging than what Eq. (8) implies. On the computational front, errors associated with the determination of each matrix element compound in the FEIR activity predictions, and those of poor accuracy, in this case the vibrational transition moments (Sec. IV B 1), could degrade the quality of prediction.

## 4. Effect of vibrational dynamics on the correlation between calculated and experimental mode-specific activities

We have attempted to address some of the sources of errors discussed above by invoking response function calculations to simulate the time-dependent FEIR spectra of nine of the coumarins shown in Fig. 2 using the methodology outlined in Sec. IV A 4 for C6. This allows us to include the contribution from vibrational dynamics and finite pulses, and eliminate the errors from the DFT-calculated vibrational transition moments by using values extracted from the FTIR spectra. Here we compare experimental mode-specific FEIR cross-sections (at $\tau_{enc} = 600$ fs) with their calculated counterparts (at $\tau_{enc} = 500$ fs) derived from response function simulations. In each case, we extract the mode-specific values by fitting each spectrum to a sum of Gaussians to extract the peak areas and report the mode-specific FEIR cross-sections (for experiment) and activities (for simulation) as fractional peak areas normalized by the total spectrum.

Figure 13 shows the relationship between the simulated and experimental mode-specific quantities at different levels of calculation. Figure 13(a) indicates the purely static case where the simulated quantities are derived entirely from the DFT-calculated matrix elements via Eq. (8). Since this is a stick spectrum, the normalized FEIR activities are calculated as $\frac{A_i}{\sum_{i=1}^{n} A_i}$, where $n$ is the total number of modes within the window of the IR pump spectrum with each activity having been scaled by its spectral intensity (Sec. II C 2). A significant improvement in the amount of scatter in the correlation is achieved in Fig. 13(b) by instead using the activities extracted from the response function simulations neglecting coherences ("population only") with IR transition dipoles extracted from FTIR spectra, as described above. Finally, in Fig. 13(c) we employ the full response function simulations with vibrational coherence included, which further improves the correlation against the experimental values. Comparisons between the experimental and simulated spectra are shown in Sec. S6.

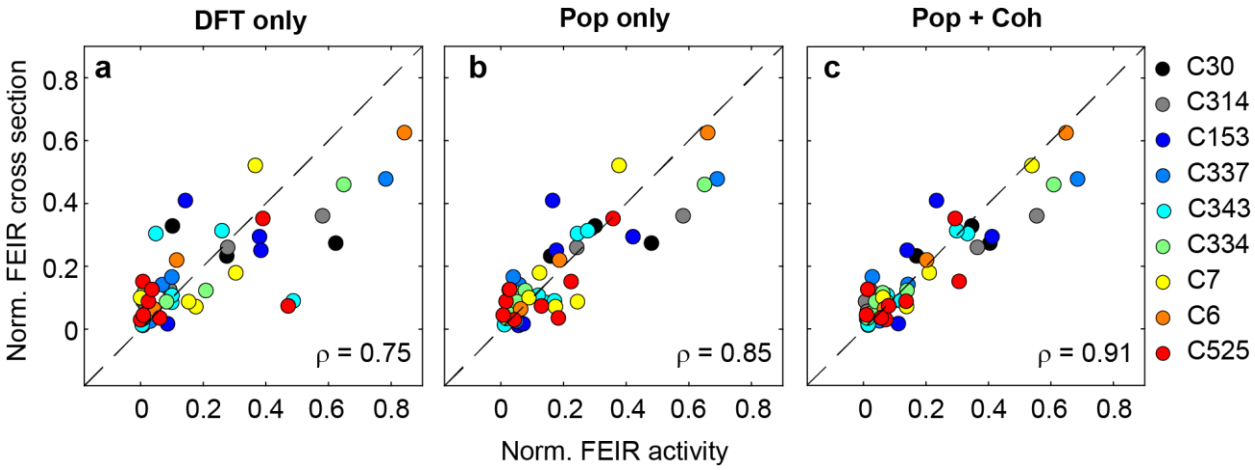


**FIG 13**. Effect of vibrational dynamics on the correlation between computed and experimental mode-specific activities. All panels use the same experimental values at $\tau_{enc}$ = 600 fs (y axis). (a) Static DFT-calculated FEIR activities (Eq. 8), normalized within the experimental IR pulse envelope. (b) Peak areas extracted from response function calculation at $\tau_{enc}$ = 500 fs neglecting coherence pahtways, and IR transition moments extracted from FTIR spectra. (c) Same as (b) but including coherence pathways.

These comparisons demonstrate the extent to which the neglect of time-dependent phenomena affects the prediction of broadband FEIR peak intensities. Additionally, replacing less accurate computed parameters (IR transition moments) with those determined from auxiliary experiments (FTIR spectra) is a useful strategy for improved prediction. A more careful comparison of simulated and experimental spectra (Fig. S6.3) indicate that the DFT calculations also reliably predict the relative signs of the FCFs and the orientational factors, which is evident through the detailed pattern of peak intensities and signs at earlier encoding delays that those investigated in Fig. 13.[26]

# V. CONCLUSIONS

In this work we have investigated the molecular factors that collectively determine a chromophore's FEIR activity. Specifically, we identified the influence of the vibrational and electronic transition dipole moments, their relative orientation, and the $\langle \mathbf{1}_j \,|\, \mathbf{0}' \rangle$ Franck-Condon factor describing their coupling. We used a DFT-based computational strategy to calculate these quantities for a variety of molecules in the coumarin family, and found that the predicted FEIR activities produces overall order of magnitude agreement with signal strengths in experiment.

One complication with assessing these computational predictions is the influence of time-dependent behavior in our FEIR experiments, arising from vibrational dynamics and especially the effect of broadband excitation pulses. To account for some of these effects we employed response function simulations of spectra and with our DFT-computed quantities as input. These simulations provide valuable insights into

the extent to which the calculations reproduce the features observed in experimental spectra. Specifically, the computations were shown to produce generally accurate predictions for molecular quantities like dipole orientation and the signs of the Franck-Condon wavefunction overlaps, which are not typically accessible in conventional methods but readily apparent in broadband FEIR spectra. We anticipate that mode-specific FEIR activities should be more readily apparent in narrow-band IR experiments, which lack vibrational coherence pathways.

Overall, the computational methodology presented in this work offers a straightforward approach to predicting FEIR activities to guide chromophore selection. The majority of the FEIR-bright vibrations in the coumarins we studied are skeletal ring modes that in general are poor reports of chemical interactions, although we note the strong carbonyl FEIR activity of C153 and C337, and provide a short discussion on the rest of the carbonyl vibrations in Sec. S8. One important goal is therefore the identification of candidate FEIR chromophores containing known reporter modes, or even the rational design of novel fluorophores for specific FEIR applications. In all these cases, we anticipate that computational strategies based on the work presented here will play a vital role.

# SUPPLEMENTARY MATERIAL

See the supplementary material for details on calculation of FCFs, electronic structure calculations, normal mode snapshots and correlations between $S$ and $|\mu|^2$, fitting of FTIR spectra, polarization dependent FEIR spectra, qualitative comparison of experimental and simulated FEIR spectra at $\tau_{enc} = 500$ fs and $\tau_{enc} = 0$ fs, comparison of geometry optimization and frequency calculations C6 using long-range corrected functional and triple zeta basis set (ωB97XD/Def2-TZVP), comparison of predicted and experimental coumarin carbonyl FEIR activities.

# ACKNOWLEDGMENTS

This work was supported by a grant from the National Science Foundation (Grant No. CHE-2155027). Steady-state electronic absorption and fluorescence characterization made use of the shared facilities at the University of Chicago Materials Research Science and Engineering Center, supported by the National Science Foundation under Award No. DMR-2011854. The authors thank Nicholas H. C. Lewis and Brennan Ashwood for their valuable feedback on the manuscript.

# AUTHOR DECLARATIONS

## Conflict of Interest

The authors have no conflicts to disclose.

## Author contributions

**Abhirup Guha:** Conceptualization (equal); Methodology (lead); Formal analysis (equal); Visualization (equal); Writing – original draft preparation (lead); Writing – review and editing (equal). **Lukas Whaley-Mayda:** Conceptualization (equal); Methodology (supporting); Formal analysis (equal); Visualization (equal); Writing—review and editing (equal). **Seung Yeon Lee:** Formal analysis (supporting); Writing – review and editing (equal); **Andrei Tokmakoff:** Conceptualization (equal); Funding acquisition (lead); Writing – review and editing (equal).

# DATA AVAILABILITY

The data that support the findings of this study are openly available in Zenodo at https://zenodo.org/doi/10.5281/zenodo.10648341.

# REFERENCES


[1] D. L. Jeanmaire, and R. P. Van Duyne, "Surface Raman spectroelectrochemistry: Part I. Heterocyclic, aromatic, and aliphatic amines adsorbed on the anodized silver electrode", Journal of Electroanalytical Chemistry and Interfacial Electrochemistry **84**, 1 (1977).
[2] M. Fleischmann, P. J. Hendra, and A. J. McQuillan, "Raman spectra of pyridine adsorbed at a silver electrode", Chemical Physics Letters **26**, 163 (1974).
[3] M. G. Albrecht, and J. A. Creighton, "Anomalously intense Raman spectra of pyridine at a silver electrode", Journal of the American Chemical Society **99**, 5215 (1977).
[4] J. Wessel, "Surface-enhanced optical microscopy", Journal of Optical Society of America B **2**, 1538 (1985).
[5] A. Laubereau, A. Seilmeier, and W. Kaiser, "A new technique to measure ultrashort vibrational relaxation times in liquid systems", Chemical Physics Letters **36**, 232 (1975).
[6] A. Seilmeier, W. Kaiser, A. Laubereau, and S. F. Fischer, "A Novel Spectroscopy Using Ultrafast Two-Pulse Excitation of Large Polyatomic Molecules", Chemical Physics Letters **58**, 225 (1978).
[7] H. J. Hübner, M. Wörner, W. Kaiser, and A. Seilmeier, "Subpicosecond vibrational relaxation of skeletal modes in polyatomic molecules", Chemical Physics Letters **182**, 315 (1991).
[8] J. C. Wright, "Double Resonance Excitation of Fluorescence in the Condensed Phase—An Alternative to Infrared, Raman, and Fluorescence Spectroscopy", Applied Spectroscopy **34**, 151 (1980).
[9] W. E. Moerner, and D. P. Fromm, "Methods of single-molecule fluorescence spectroscopy and microscopy", Review of Scientific Instruments **74**, 3597 (2003).
[10] S. Weiss, "Measuring conformational dynamics of biomolecules by single molecule fluorescence spectroscopy", Nat. Struct. Biol. **7**, 724 (2000).

[11] B. Schuler, "Single-Molecule Fluorescence Spectroscopy of Protein Folding", ChemPhysChem **6**, 1206 (2005).
[12] T. Ha, A. Y. Ting, J. Liang, W. B. Caldwell, A. A. Deniz, D. S. Chemla, P. G. Schultz, and S. Weiss, "Single-molecule fluorescence spectroscopy of enzyme conformational dynamics and cleavage mechanism", Proceedings of the National Academy of Sciences **96**, 893 (1999).
[13] H. Xiong, and W. Min, "Combining the best of two worlds: Stimulated Raman excited fluorescence", J. Chem. Phys. **153**, 210901 (2020).
[14] H. Xiong, N. Qian, Y. Miao, Z. Zhao, and W. Min, "Stimulated Raman Excited Fluorescence Spectroscopy of Visible Dyes", J. Phys. Chem. Lett. **10**, 3563 (2019).
[15] H. Xiong, L. Shi, L. Wei, Y. Shen, R. Long, Z. Zhao, and W. Min, "Stimulated Raman excited fluorescence spectroscopy and imaging", Nature Photonics **13**, 412 (2019).
[16] L. Whaley-Mayda, S. B. Penwell, and A. Tokmakoff, "Fluorescence-Encoded Infrared Spectroscopy: Ultrafast Vibrational Spectroscopy on Small Ensembles of Molecules in Solution", J. Phys. Chem. Lett. **10**, 1967 (2019).
[17] L. Whaley-mayda, A. Guha, S. B. Penwell, and A. Tokmakoff, "Fluorescence-Encoded Infrared Vibrational Spectroscopy with Single-Molecule Sensitivity", J. Am. Chem. Soc. **143**, 10 (2021).
[18] L. Whaley-Mayda, A. Guha, and A. Tokmakoff, "Resonance conditions, detection quality, and single-molecule sensitivity in fluorescence-encoded infrared vibrational spectroscopy", J. Chem. Phys. **156**, 174202 (2022).
[19] J. N. Mastron, and A. Tokmakoff, "Two-Photon-Excited fluorescence-Encoded infrared spectroscopy", Journal of Physical Chemistry A **120**, 9178 (2016).
[20] H. Wang, D. Lee, Y. Cao, X. Bi, J. Du, K. Miao, and L. Wei, "Bond-selective fluorescence imaging with single-molecule sensitivity", Nature Photonics **17**, 846 (2023).
[21] R. Chikkaraddy, R. Arul, L. A. Jakob, and J. J. Baumberg, "Single-molecule mid-infrared spectroscopy and detection through vibrationally assisted luminescence", Nature Photonics **17**, 865 (2023).
[22] X. Liu, J. M. Cole, and Z. Xu, "Substantial Intramolecular Charge Transfer Induces Long Emission Wavelengths and Mega Stokes Shifts in 6-Aminocoumarins", The Journal of Physical Chemistry C **121**, 13274 (2017).
[23] X. Liu, J. M. Cole, P. G. Waddell, T.-C. Lin, J. Radia, and A. Zeidler, "Molecular Origins of Optoelectronic Properties in Coumarin Dyes: Toward Designer Solar Cell and Laser Applications", The Journal of Physical Chemistry A **116**, 727 (2012).
[24] X. Liu, Z. Xu, and J. M. Cole, "Molecular Design of UV–vis Absorption and Emission Properties in Organic Fluorophores: Toward Larger Bathochromic Shifts, Enhanced Molar Extinction Coefficients, and Greater Stokes Shifts", The Journal of Physical Chemistry C **117**, 16584 (2013).
[25] L. Whaley-Mayda, A. Guha, and A. Tokmakoff, "Multimode vibrational dynamics and orientational effects in fluorescence-encoded infrared spectroscopy. I. Response function theory", J. Chem. Phys. **159**, (2023).
[26] L. Whaley-Mayda, A. Guha, and A. Tokmakoff, "Multimode vibrational dynamics and orientational effects in fluorescence-encoded infrared spectroscopy. II. Analysis of early-time signals", J. Chem. Phys. **159**, (2023).
[27] J. D. Gaynor, R. B. Weakly, and M. Khalil, "Multimode two-dimensional vibronic spectroscopy. I. Orientational response and polarization-selectivity", J. Chem. Phys. **154**, (2021).
[28] F. Santoro, A. Lami, R. Improta, and V. Barone, "Effective method to compute vibrationally resolved optical spectra of large molecules at finite temperature in the gas phase and in solution", Journal of Chemical Physics **126**, (2007).
[29] J. Von Cosel, J. Cerezo, D. Kern-Michler, C. Neumann, L. J. G. W. Van Wilderen, J. Bredenbeck, F. Santoro, and I. Burghardt, "Vibrationally resolved electronic spectra including vibrational pre-excitation: Theory and application to VIPER spectroscopy", Journal of Chemical Physics **147**, (2017).

[30] P. T. Ruhoff, "Recursion relations for multi-dimensional Franck-Condon overlap integrals", Chemical Physics **186**, 355 (1994).
[31] T. E. Sharp, and H. M. Rosenstock, "Franck—Condon Factors for Polyatomic Molecules", J. Chem. Phys. **41**, 3453 (1964).
[32] J. Lermé, "Iterative methods to compute one- and two-dimensional Franck-Condon factors. Tests of accuracy and application to study indirect molecular transitions", Chemical Physics **145**, 67 (1990).
[33] Gaussian 09, Revision B.01, M. J. Frisch, G. W. Trucks, H. B. Schlegel, G. E. Scuseria, M. A. Robb, J. R. Cheeseman, G. Scalmani, V. Barone, G. A. Petersson, H. Nakatsuji, X. Li, M. Caricato, A. Marenich, J. Bloino, B. G. Janesko, R. Gomperts, B. Mennucci, H. P. Hratchian, J. V. Ortiz, A. F. Izmaylov, J. L. Sonnenberg, D. Williams-Young, F. Ding, F. Lipparini, F. Egidi, J. Goings, B. Peng, A. Petrone, T. Henderson, D. Ranasinghe, V. G. Zakrzewski, J. Gao, N. Rega, G. Zheng, W. Liang, M. Hada, M. Ehara, K. Toyota, R. Fukuda, J. Hasegawa, M. Ishida, T. Nakajima, Y. Honda, O. Kitao, H. Nakai, T. Vreven, K. Throssell, J. J. A. Montgomery, J. E. Peralta, F. Ogliaro, M. Bearpark, J. J. Heyd, E. Brothers, K. N. Kudin, V. N. Staroverov, T. Keith, R. Kobayashi, J. Normand, K. Raghavachari, A. Rendell, J. C. Burant, S. S. Iyengar, J. Tomasi, M. Cossi, J. M. Millam, M. Klene, C. Adamo, R. Cammi, J. W. Ochterski, R. L. Martin, K. Morokuma, O. Farkas, J. B. Foresman, and D. J. Fox, (2016),
[34] A. Becke, "Density-functional thermochemistry. III. The role of exact exchange", J. Chem. Phys **98**, 5648 (1993).
[35] P. J. Stephens, F. J. Devlin, C. F. Chabalowski, and M. J. Frisch, "Ab Initio Calculation of Vibrational Absorption and Circular Dichroism Spectra Using Density Functional Force Fields", The Journal of Physical Chemistry **98**, 11623 (1994).
[36] D. Jacquemin, V. Wathelet, E. A. Perpete, and C. Adamo, "Extensive TD-DFT benchmark: singlet-excited states of organic molecules", Journal of Chemical Theory and Computation **5**, 2420 (2009).
[37] J.-D. Chai, and M. Head-Gordon, "Systematic optimization of long-range corrected hybrid density functionals", J. Chem. Phys. **128**, 084106 (2008).
[38] M. I. Sorour, A. H. Marcus, and S. Matsika, "Modeling the Electronic Absorption Spectra of the Indocarbocyanine Cy3", Molecules **27**, 4062 (2022).
[39] NIST Computational Chemistry Comparison and Benchmark DataBase, NIST Standard Reference Database 101, (2022), https://cccbdb.nist.gov/vibscalejust.asp
[40] D. Jacquemin, B. Mennucci, and C. Adamo, "Excited-state calculations with TD-DFT: from benchmarks to simulations in complex environments", Physical Chemistry Chemical Physics **13**, 16987 (2011).
[41] S. Manzhos, H. Segawa, and K. Yamashita, "Computational dye design by changing the conjugation order: Failure of LR-TDDFT to predict relative excitation energies in organic dyes differing by the position of the methine unit", Chemical Physics Letters **527**, 51 (2012).
[42] D. Jacquemin, and C. Adamo, "Bond length alternation of conjugated oligomers: wave function and DFT benchmarks", Journal of chemical theory and computation **7**, 369 (2011).

# Supplementary Material for

# Molecular factors determining brightness in Fluorescence-Encoded Infrared vibrational spectroscopy

Abhirup Guha,[1] Lukas Whaley-Mayda,[1] Seung Yeon Lee,[1] and Andrei Tokmakoff[1]

*Department of Chemistry, James Franck Institute, and Institute of Biophysical Dynamics,*

*The University of Chicago, Chicago, Illinois 60637, USA*

## Contents

| Topic | Page |
|---|---|
| **S1.** Vibronic coupling | 2 |
| **A.** Calculation of Franck-Condon factors | 2 |
| **B.** Effect of dimension on 0-0 overlap integrals | 6 |
| **S2.** Franck-Condon factors as a function of Huang-Rhys factors | 8 |
| **S3.** IR intensities and Huang-Rhys factors of coumarin normal modes in 6 $\mu m$ region | 9 |
| **S4.** Fit results for extracting integrated extinction coefficients of vibrations from FTIRs of coumarins | 22 |
| **S5.** Experimental determination of normal mode anisotropy | 25 |
| **S6.** Comparison of experimental and simulated FEIR spectra | 27 |
| **S7.** Comparison of results using different functionals (Coumarin 6) | 29 |
| **S8.** Computational predictions of FEIR activities of carbonyl modes in coumarins | 30 |

# S1. Vibronic coupling

## A. Calculation of Franck-Condon factors

*Much of the theory for this section has been presented in section IIB of the main text. Here, we present the details of the theory of the FCFs systematically for the reference of the reader, including details that were not mentioned in the main text. For further reading, reader can go through the detailed derivation of the recursion relations given by Ruhoff in ref. 1, and presented concisely by Santoro et. al. in the appendix of ref. 2.*

The encoding transition, that is, the transition from the excited vibrational state in the electronic ground state to the electronic excited state requires coupling between the vibrational states of the ground and the excited electronic states. To understand the nature of the encoding transition, we must approach the vibronic coupling with suitable approximations. As the first level of approximation, we treat the light-matter interaction with first-order perturbation theory. Therefore, we describe the total Hamiltonian as:

$$H = H_0 + V \tag{1.1}$$

Where, $\boldsymbol{H_0}$ is the unperturbed Hamiltonian, while $\boldsymbol{V}$ describes the perturbation, which under the semi-classical treatment, is given as

$$V = -\mu \cdot E \tag{1.2}$$

Here, $\boldsymbol{\mu}$ is the electronic dipole moment of the molecule that interacts with the electric field, $\boldsymbol{E}$ of the perturbing radiation.

The encoding transition dipole is then described by

$$\mu_{eg} = \langle \Psi_G \,|\, \mu \,|\, \Psi_E \rangle \tag{1.3}$$

where $\Psi_G$ and $\Psi_E$ are wavefunctions describing the molecule in the ground and excited states, respectively. Under the Born-Oppenheimer approximation, these can be factored into wavefunctions of the electronic and the nuclear coordinates

$$\Psi_G = \psi_g \cdot \chi_v(Q)$$

We also explicitly write out the molecular dipole moment as a Taylor series expansion about the equilibrium geometry in either the ground or the excited electronic state.

$$\mu = \mu_0 + \sum_{i=1}^{N}\left(\frac{\partial \mu}{\partial Q_i}\right)_0 Q_i + \frac{1}{2}\sum_{i=1}^{N}\sum_{j=1}^{N}\left(\frac{\partial^2 \mu}{\partial Q_i \partial Q_j}\right)_0 Q_i Q_j + \cdots \tag{1.4}$$

where, $N$ is the number of normal modes of the molecule. At this stage, we apply the Condon approximation, that is, we assume that the electronic transitions are vertical, and thus neglect the terms containing dependence on the nuclear coordinates. This truncates the expansion to the first term, and under this approximation, the vibronic transition dipole (Eq. 1.3) can be written as,

$$\mu_{eg} = \langle \psi_g \,|\, \mu_0 \,|\, \psi_e \rangle \cdot \langle \chi_{\mathbf{v}} \,|\, \chi_{\mathbf{v}'} \rangle \tag{1.5}$$

describing a transition from the $v^{th}$ vibrational state in the electronic ground state to the $v'^{th}$ vibrational state in the electronic excited state. Here, the multidimensional Franck-Condon (FC) factors, written more explicitly, are

$$\langle \chi_{\mathbf{v}} \,|\, \chi_{\mathbf{v}'} \rangle = \langle \chi_{v_1}, \chi_{v_2}, \cdots, \chi_{v_N} \,|\, \chi_{v_1'}, \chi_{v_2'}, \cdots, \chi_{v_N'} \rangle \tag{1.6}$$

Note that we use primed notation for describing the normal coordinate of the electronic excited state ( $\mathbf{Q'}$ ) while the unprimed notation denotes the normal coordinates of the electronic ground state ( $\mathbf{Q}$ ). The sets of normal coordinates are related to each other by the following linear transformation [ref Barone and Santoro's papers]:

$$\mathbf{Q} = \mathbf{J}\mathbf{Q'} + \mathbf{K} \tag{1.7}$$

where, $\mathbf{J}$, the Duschinsky matrix is a $(N \times N)$ dimensional matrix that reflects the difference in the normal mode character between the ground and the excited electronic states. $\mathbf{K}$ is a $N$ dimensional vector, describing the displacements of the electronic excited state potential along the normal coordinates of the $N$ vibrational modes of the molecule. These vectors are defined as:

$$\begin{aligned} \mathbf{J} &= \mathbf{L}^{-1}\mathbf{L}' \\ \mathbf{K} &= \mathbf{L}^{-1}(\mathbf{q}'^{0} - \mathbf{q}^{0}) \end{aligned} \tag{1.8}$$

The $\mathbf{L}$ matrix transforms the mass-weighted cartesian coordinates $q$ to normal coordinates $\mathbf{Q}$ according to the following linear transformation:

$$\mathbf{Q} = \mathbf{L}^{-1}(q - q^{0}) \tag{1.9}$$

where, $\boldsymbol{q}^{\mathbf{0}}$ represents the cartesian coordinates pertaining to the equilibrium geometry of the molecule. In the context of FEIR spectroscopy, we also assume that visible encoding pulse delivers sufficient energy to promote the molecule to the ground vibrational state of the excited electronic state. The higher vibrational states are not accessed. Under this assumption, the FC factors for those normal modes excited by the IR pump pulse are simplified as $\langle \chi_{\mathbf{1}} \mid \chi_{\mathbf{0'}} \rangle$. For the IR excitation of a single normal mode, the multidimensional FC factor would read as $\langle \chi_{v_1=0}, \chi_{v_2=0}, \cdots, \chi_{v_k=1}, \cdots \chi_{v_N=0} \mid \chi_{v_{1'}=0}, \chi_{v_{2'}=0}, \cdots, \chi_{v_{k'}=0}, \cdots \chi_{v_{N'}=0} \rangle$, which implies that the $k^{th}$ normal mode is excited to $v=1$ state by the IR pulse, leaving all the other N-1 modes in the vibrational ground state. The encoding pulse excites all the normal modes to the vibrational ground state in the electronic excited state. The magnitude of these factors is affected by the displacement of the excited state potential along the normal coordinates of the ground state molecular vibrations, differences in vibrational frequencies between the electronic ground and excited states, and Duschinsky mixing.

The multidimensional $\langle \chi_{\mathbf{0}} \mid \chi_{\mathbf{0'}} \rangle$ FC integral is shown to be exactly solvable, and all the other FC integrals can be solved with recursion relations using the value of the $\langle \chi_{\mathbf{0}} \mid \chi_{\mathbf{0'}} \rangle$ integral. We will not go into the derivation, which is shown in detail elsewhere[1], but for completeness, we will summarize all the necessary expressions here. The complete multidimensional $\langle \chi_{\mathbf{0}} \mid \chi_{\mathbf{0'}} \rangle$ FC integral is derived to be:

$$\langle \chi_{\mathbf{0}} \mid \chi_{\mathbf{0'}} \rangle = (\det\boldsymbol{\Omega}\det\boldsymbol{\Omega}')^{1/4} \left( \frac{2^N \det \mathbf{J}}{\det \mathbf{X}} \right)^{1/2} \times \exp\left[ -\frac{1}{2}\mathbf{K}^{\dagger}\boldsymbol{\Omega}\mathbf{K} + \frac{1}{2}\mathbf{Y}^{\dagger}\mathbf{X}^{-1}\mathbf{Y} \right] \tag{1.10}$$

where, $\boldsymbol{\Omega}$'s are diagonal matrices of ground state and excited state normal mode frequencies, $\mathbf{X}$ and $\mathbf{Y}$ are matrices given as:

$$\begin{aligned} \mathbf{Y} &= \mathbf{J}^{\dagger}\boldsymbol{\Omega}\mathbf{K} \\ \mathbf{X} &= \mathbf{J}^{\dagger}\boldsymbol{\Omega}\mathbf{J} + \boldsymbol{\Omega}' \end{aligned} \tag{1.11}$$

The recursion relation to compute a generalized FC factor, $\langle \chi_{\mathbf{v}} \mid \chi_{\mathbf{v'}} \rangle$ is given as follows:

$$\begin{aligned}\langle \chi_{\mathbf{v}} \mid \chi_{\mathbf{v}'} \rangle = & \left(\frac{1}{2v_k}\right)^{1/2} B_k \langle \chi_{\mathbf{v}-1_k} \mid \chi_{\mathbf{v}'} \rangle + \left(\frac{v_k - 1}{v_k}\right)^{1/2} E_{kk} \langle \chi_{\mathbf{v}-2_k} \mid \chi_{\mathbf{v}'} \rangle \\ & + \sum_{l \neq k} \left(\frac{v_l}{v_k}\right)^{1/2} E_{kl} \langle \chi_{\mathbf{v}-1_k-1_l} \mid \chi_{\mathbf{v}'} \rangle \\ & + \sum_{l} \left(\frac{v_l'}{v_k}\right)^{1/2} F_{kl} \langle \chi_{\mathbf{v}-1_k} \mid \chi_{\mathbf{v}'-1_l} \rangle \end{aligned} \tag{1.12}$$

where, $\mathbf{B}$, $\mathbf{E}$ and $\mathbf{F}$ are Sharp and Rosenstock matrices[3], revised and corrected forms of which were presented in the appendix section of Ref. 2.

$$\begin{aligned}\mathbf{B} &= 2\mathbf{K}^{\dagger}\boldsymbol{\Omega}^{1/2}(1 - \boldsymbol{\Omega}^{1/2}\mathbf{J}\mathbf{X}^{-1}\mathbf{J}^{\dagger}\boldsymbol{\Omega}^{1/2}) \\ \mathbf{E} &= 2\boldsymbol{\Omega}^{1/2}\mathbf{J}\mathbf{X}^{-1}\mathbf{J}^{\dagger}\boldsymbol{\Omega}^{1/2} - \mathbf{I} \\ \mathbf{F} &= 2\boldsymbol{\Omega}^{1/2}\mathbf{J}\mathbf{X}^{-1}\boldsymbol{\Omega}'^{1/2}\end{aligned} \tag{1.13}$$

In the context of FEIR spectroscopy, the FC factor of interest is $\langle \chi_{\mathbf{0}+1_k} \mid \chi_{\mathbf{0}'} \rangle$ which implies the multidimensional FC overlap between the electronic ground state (where all but the $k^{th}$ normal mode are in the vibrational ground state) and the electronic excited state where all the normal modes are in the vibrational ground state. In this picture, only the first term of the RHS of Eq. (1.4) survives, while the others are null. The expression for the FC integral of our interest, which is the same as the FC factors that govern the transition strength in VIPER spectroscopy[4], is given as follows,

$$\langle \chi_{\mathbf{0}+1_k} \mid \chi_{\mathbf{0}'} \rangle = \frac{1}{\sqrt{2}} B_k \langle \chi_{\mathbf{0}} \mid \chi_{\mathbf{0}'} \rangle \tag{1.14}$$

Let us treat these multidimensional FC factors at three different levels of approximation. This will help us understand the effect of the various parameters, namely, the Duschinsky mixing, the different vibrational frequencies in the electronic ground and excited states, and the displacement of the excited state potential along the normal coordinates of the vibrational modes.

**Approximation I:** FC factors as a function of only the displacements of the excited state potential along the normal coordinates of the molecular vibrations with no change in vibrational frequencies between the ground and the excited electronic states (i.e. $\boldsymbol{\Omega} = \boldsymbol{\Omega}'$) and no mode mixing (considering $\mathbf{J} = \mathbf{I}$) —the multidimensional overlap integrals can be written as a product of the 1-dimensional FC factors for each normal mode,

$$\langle \chi_{\mathbf{0}+1_k} \mid \chi_{\mathbf{0}'} \rangle = \langle \chi_{v_1=0} \mid \chi_{v_1'=0} \rangle \langle \chi_{v_2=0} \mid \chi_{v_2'=0} \rangle \cdots \langle \chi_{v_k=1} \mid \chi_{v_k'=0} \rangle \cdots \langle \chi_{v_N=0} \mid \chi_{v_N'=0} \rangle \tag{1.15}$$

The 0-0 overlap integral, under this approximation, is written as,

$$\langle \chi_{\mathbf{0}} \mid \chi_{\mathbf{0'}} \rangle = \langle \chi_{v_1=0} \mid \chi_{v_{1'}=0} \rangle \cdots \langle \chi_{v_N=0} \mid \chi_{v_{N'}=0} \rangle = \prod_{j=1}^{N} \exp\left[ -\frac{1}{2} S_j \right] \tag{1.16}$$

It can be shown that the 1-dimensional FC integrals are

$$\langle \chi_{v_j=1} \mid \chi_{v_{j'}=0} \rangle_{Approx.I} = \frac{\delta_j}{\sqrt{2}} e^{-\frac{1}{2}S_j} \tag{1.17}$$

where, $\boldsymbol{S}_j$ is the Huang-Rhys factor corresponding to the $j^{th}$ normal mode, and $\delta_j$ is the dimensionless displacement. The $\boldsymbol{\delta}$ vector is given as

$$\boldsymbol{\delta} = \mathbf{K}^T \boldsymbol{\Omega}_g^{1/2} \tag{1.18}$$

To understand the effect of the other parameters, namely, the difference in normal mode frequencies in the electronic ground and excited states, and, mode mixing, we look at two more levels of approximation

**Approximation II:** FC factors as a function of both the displacements along the normal coordinates, as well as the difference in vibrational frequencies in the electronic ground and excited states, i.e. the condition, $\mathbf{J} = \mathbf{I}$ still persists, while now we have $\boldsymbol{\Omega} \neq \boldsymbol{\Omega}'$ -- under this approximation, we can still write out the multidimensional FC integral as a product of the individual 1-dimensional FC factors. The multidimensional 0-0 overlap integral, and the 1-dimensional FC overlap integrals can be shown to be:

$$\langle \chi_{\mathbf{0}} \mid \chi_{\mathbf{0'}} \rangle = \langle \chi_{v_1=0} \mid \chi_{v_{1'}=0} \rangle \cdots \langle \chi_{v_N=0} \mid \chi_{v_{N'}=0} \rangle = \prod_{j=1}^{N} \sqrt{\frac{2\sqrt{\omega_j \cdot \omega_{j'}}}{\omega_j + \omega_{j'}}} \exp\left[ -S_j \left( 1 - \frac{\omega_{jj}}{\omega_{jj} + \omega_{j'j'}} \right) \right] \tag{1.19}$$

$$\langle \chi_{v_j=1} \mid \chi_{v_{j'}=0} \rangle_{Approx.II} = \sqrt{2}\delta_j \left( 1 - \frac{\omega_{jj}}{\omega_{jj} + \omega_{j'j'}} \right) \sqrt{\frac{2\sqrt{\omega_j \cdot \omega_{j'}}}{\omega_j + \omega_{j'}}} \exp\left[ -S_j \left( 1 - \frac{\omega_{jj}}{\omega_{jj} + \omega_{j'j'}} \right) \right] \tag{1.20}$$

Where $\omega$ is an individual frequency element in the diagonal frequency matrix $\boldsymbol{\Omega}$.

**Approximation III** The last part of this treatment is where we consider a non-unity Duschinsky matrix, and perform a complete computation of the multidimensional Franck-Condon integrals, described by Eq. (1.14).

The FCFs at Level I for vibrations >1000 $cm^{-1}$ lie within 2% of the values computed at Levels II and III of approximation, as shown in FIG S1.1.

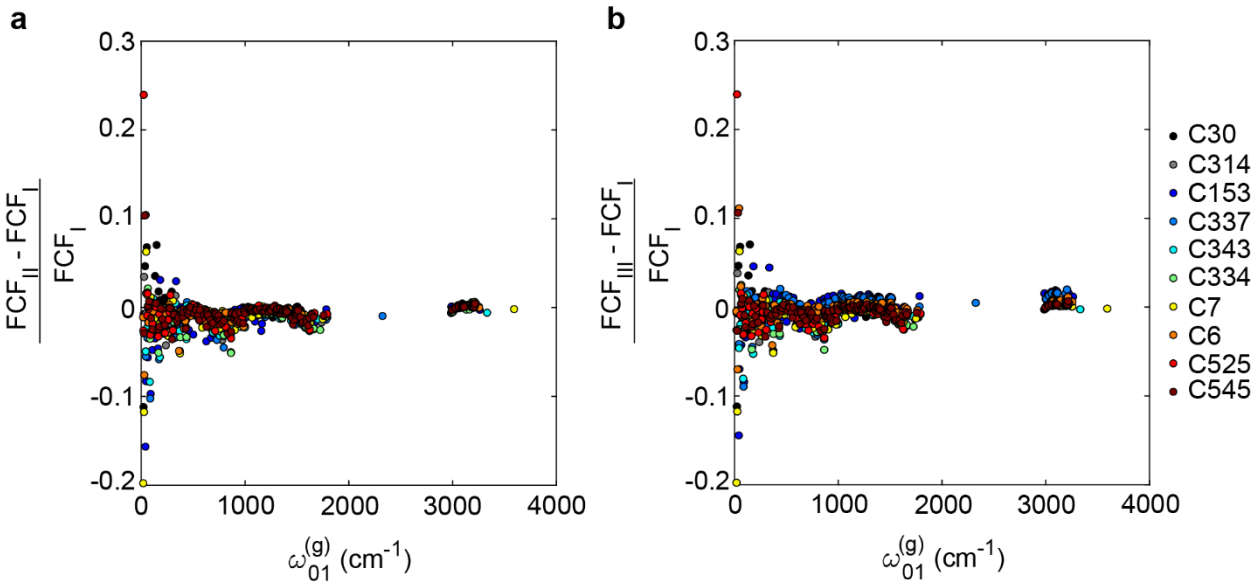


**FIG S1.1.** Difference in FCF magnitudes associated with computation at levels II (a) and III (b) relative to level I of approximation

## B. Effect of dimension on the 0-0 overlap integrals

In Fig. S1.2 below, we show the magnitude of the 0-0 overlap integrals of all ten coumarins as a function of the number of normal modes included in their calculation, starting with the highest frequency normal mode, gradually increasing the dimensions as we include the lower frequencies. Especially for C30, there are huge displacements of the excited state minimum along the coordinates of the low frequency modes. This lowers the magnitude of the overall FCFs. In the context of FEIR spectroscopy, these low frequency modes below 900 cm-1 fall way beyond the pump region, and thereby, are not excited. Moreover, these modes primarily contribute to the overall broadening of the electronic absorption lineshape, not playing any significant role in the FEIR response. We therefore restrict the dimension to the number of normal modes within the IR pulse envelope. In principle, we could include the higher frequency modes, but they have little or no impact on the integrals, as seen from the plot.

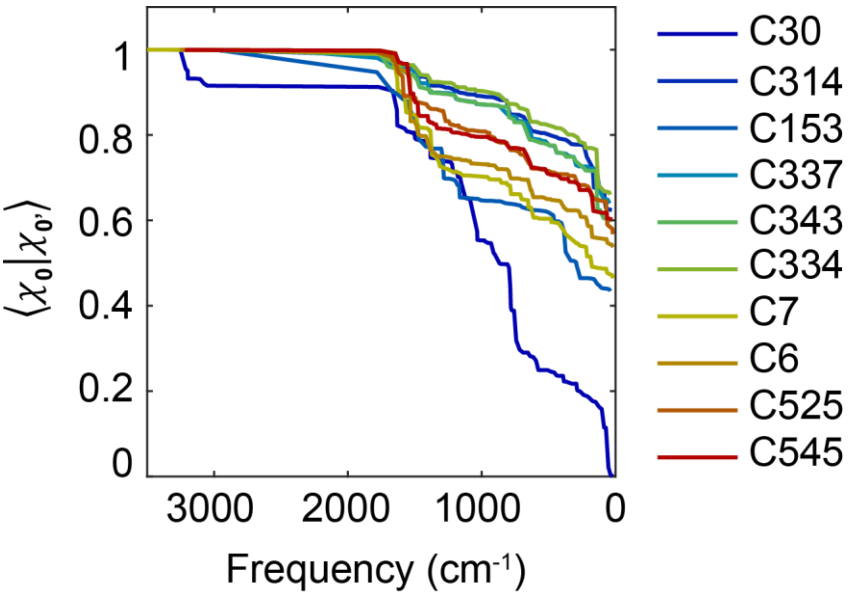


**FIG S1.2.** Magnitude of 0-0 overlap integrals as a function of dimension. Barring C30 (dark blue), the high frequency normal modes have negligible effect on the integral while the displacements along the low-frequency vibrations are large enough to bring down the value. The integrals used in the calculations are computed by reducing the dimension to the number of modes within the IR pulse envelope

## S2. Franck-Condon factors as a function of Huang-Rhys factors

The efficiency of the encoding transition is shaped by the magnitude of the Franck-Condon factor corresponding to a vibrational mode. Fig. S2 depicts how the magnitude of these integrals depends on the final vibronic states and the Huang-Rhys factors. In our study, we have assumed the $|\chi_1\rangle \rightarrow |\chi_{0'}\rangle$ (blue arrow in Fig. S2 (a) and blue line in Fig. S2 (b)) to be the only relevant vibronic transition, considering that transitions to the higher lying vibrational quanta in the excited electronic state are eliminated by the choice of our resonance condition. The square of the FCF corresponding to this transition shows a Poissonian distribution with the Huang-Rhys factor, as dictated by Eq. (1.17), maximizing at $S=1$. For organic molecules like the coumarins and acridines used in this work, the S values lie below 0.1 where the square of the FCF shows a near-linear dependence on S (Inset in Fig. S2 (b)). This makes it possible to represent the FCFs of normal modes from their corresponding Huang-Rhys factors.

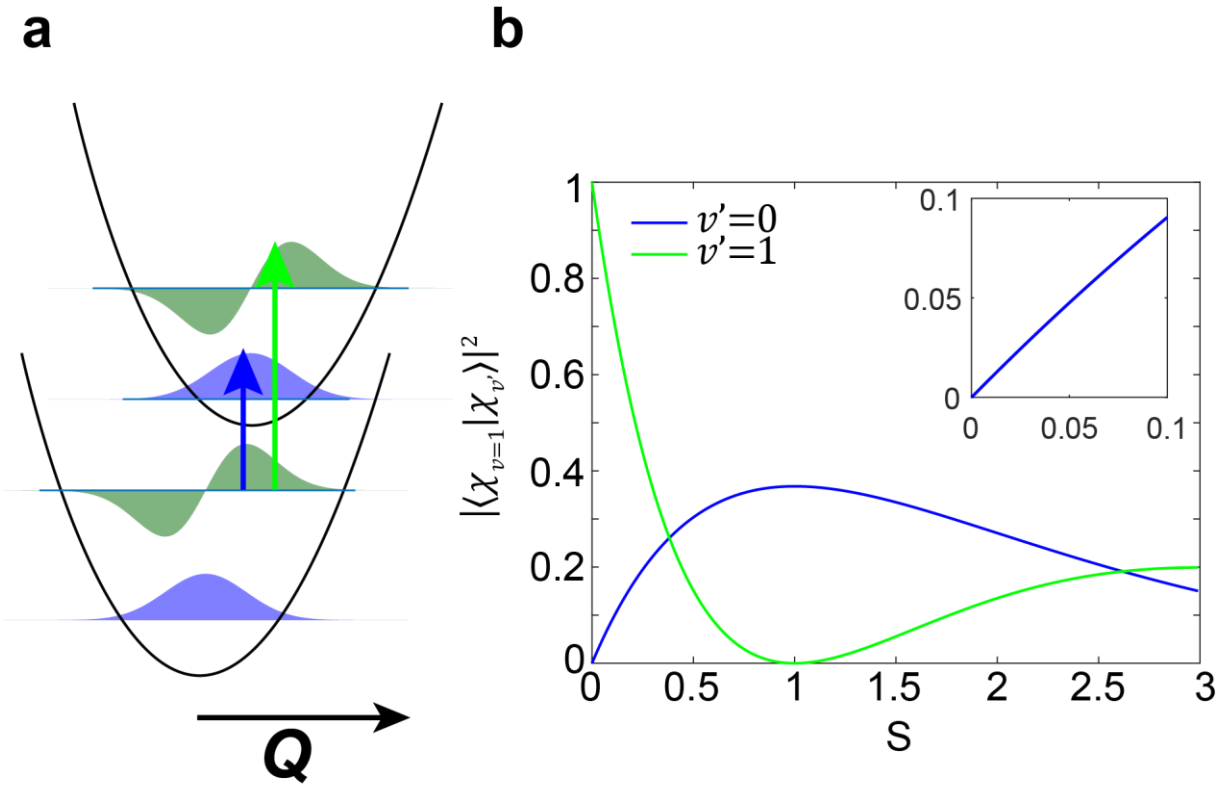


**FIG S2.** Dependence of Franck-Condon overlap integrals on the Huang-Rhys factor and the final vibrational quantum. (a) A graphical representation of three vibronic transitions originating from v=1 in the ground electronic state to $v' = 0$ (blue) and $v' = 1$ (green) in the excited electronic state. (b) Plot showing the magnitude of the squares of FCF corresponding to the two transitions shown in (a) as a function of Huang-Rhys factor. In FEIR spectroscopy, the most relevant vibronic transition as per the assumptions made is $v = 1 \rightarrow v' = 0$ (blue) that shows a Poissonian distribution, maximizing at $S = 1$. The trend within $S = 0.1$ is near-linear (Inset).

## S3. IR intensities and Huang-Rhys factors of coumarin normal modes in the 6 $\mu m$ region

This section contains the results of geometry optimization, frequency calculation, calculation of Huang-Rhys factors and their correlation with the squares of vibrational transition dipoles for all normal modes of all the coumarins studied. The snapshots of the normal modes shown for each coumarin (Fig. S3.1 – S3.10) are the ones that lie within the spectral window of the IR pump pulse and have a significant $S|\mu|^2$ (>10 km mol$^{-1}$). The exception is Fig. S3.8 that shows the two normal modes of C6 which are predicted to have strong FEIR activity but are not experimentally verified since they lie outside the spectral window of the IR pump used in the FEIR experiments. The C6 normal modes contributing to its FEIR response under our experimental conditions are shown in Fig. 1b of the main text. The color-coded arrows in each snapshot denote the respective atomic displacements corresponding to the normal mode and the red arrow represents the vibrational transition dipole. The lengths of the red arrows are arbitrary, not to be

quantitatively mapped to the IR intensity. The lengths of the color-coded arrows are also arbitrary, but the relative lengths are directly proportional to the corresponding atomic displacements.

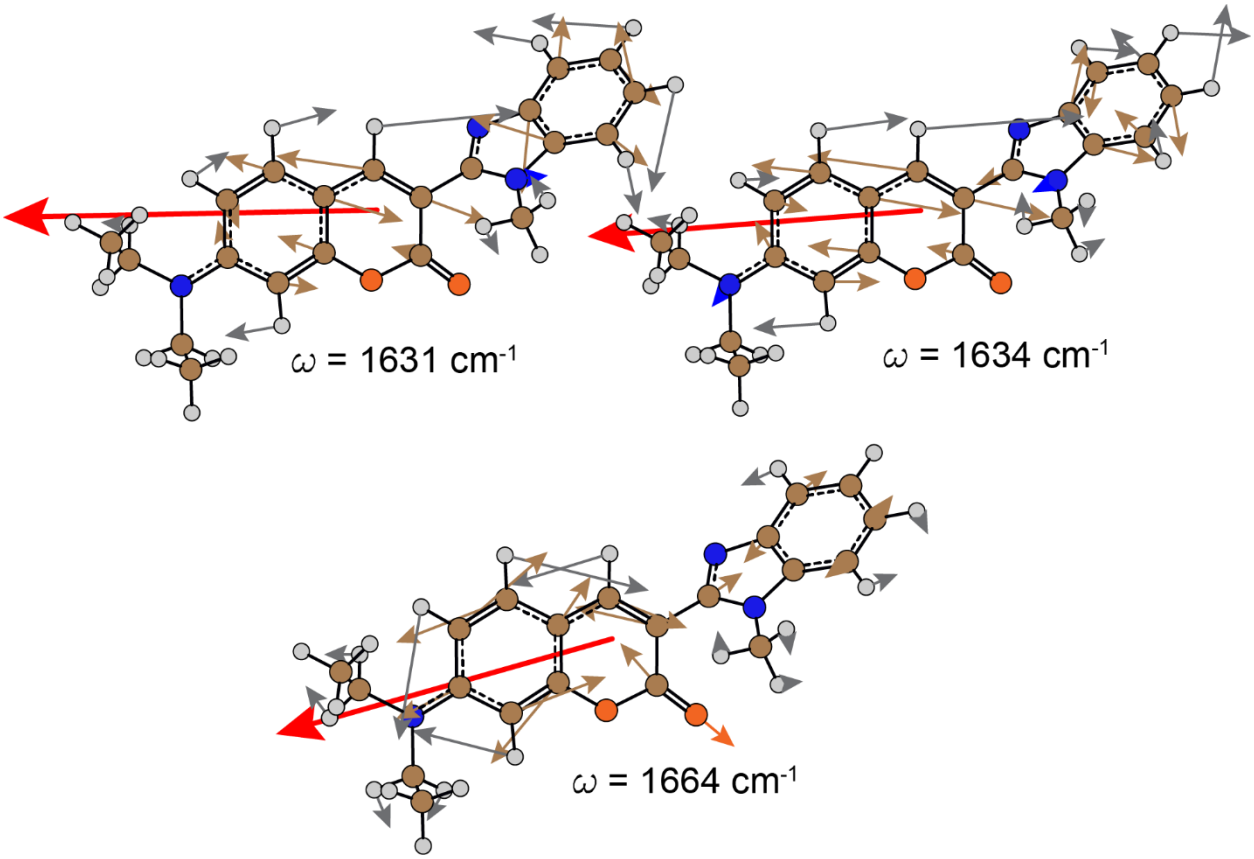


**FIG S3.1.** Snapshots of the normal modes of coumarin 30 in the spectral window of the IR pump pulse

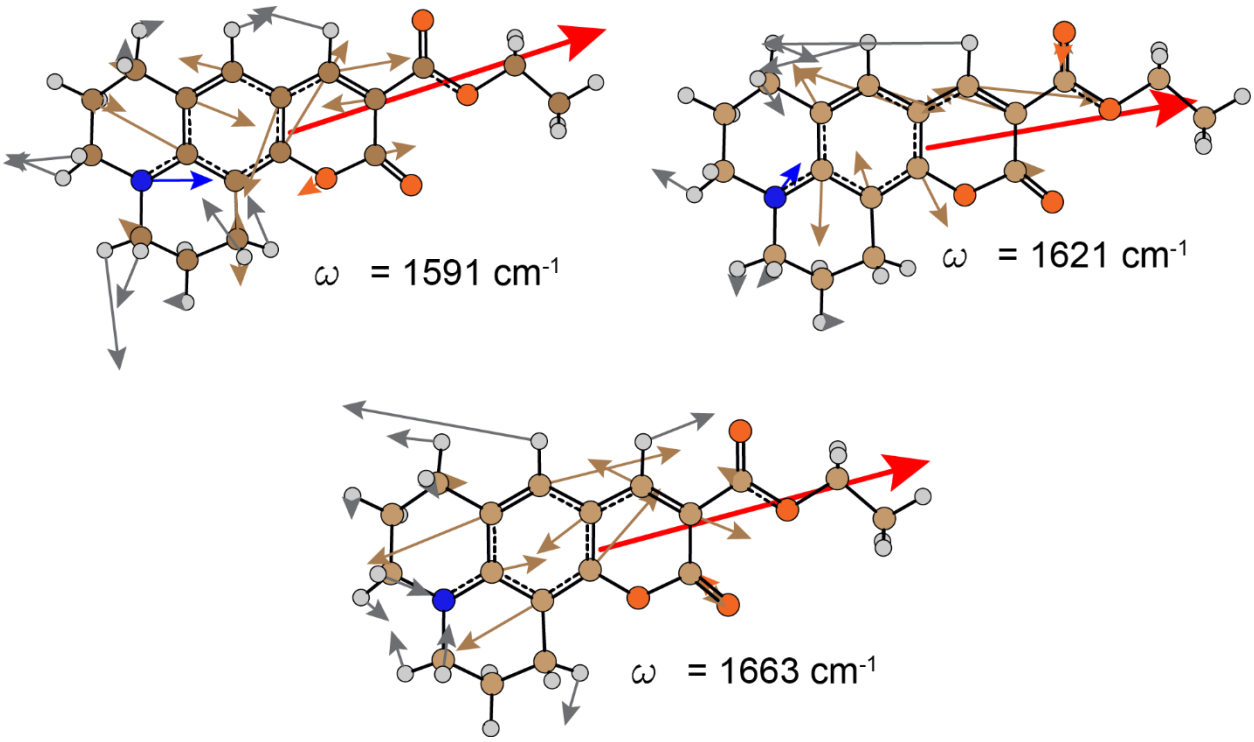


**FIG S3.2.** Snapshots of the normal modes of coumarin 314 in the spectral window of the IR pump pulse

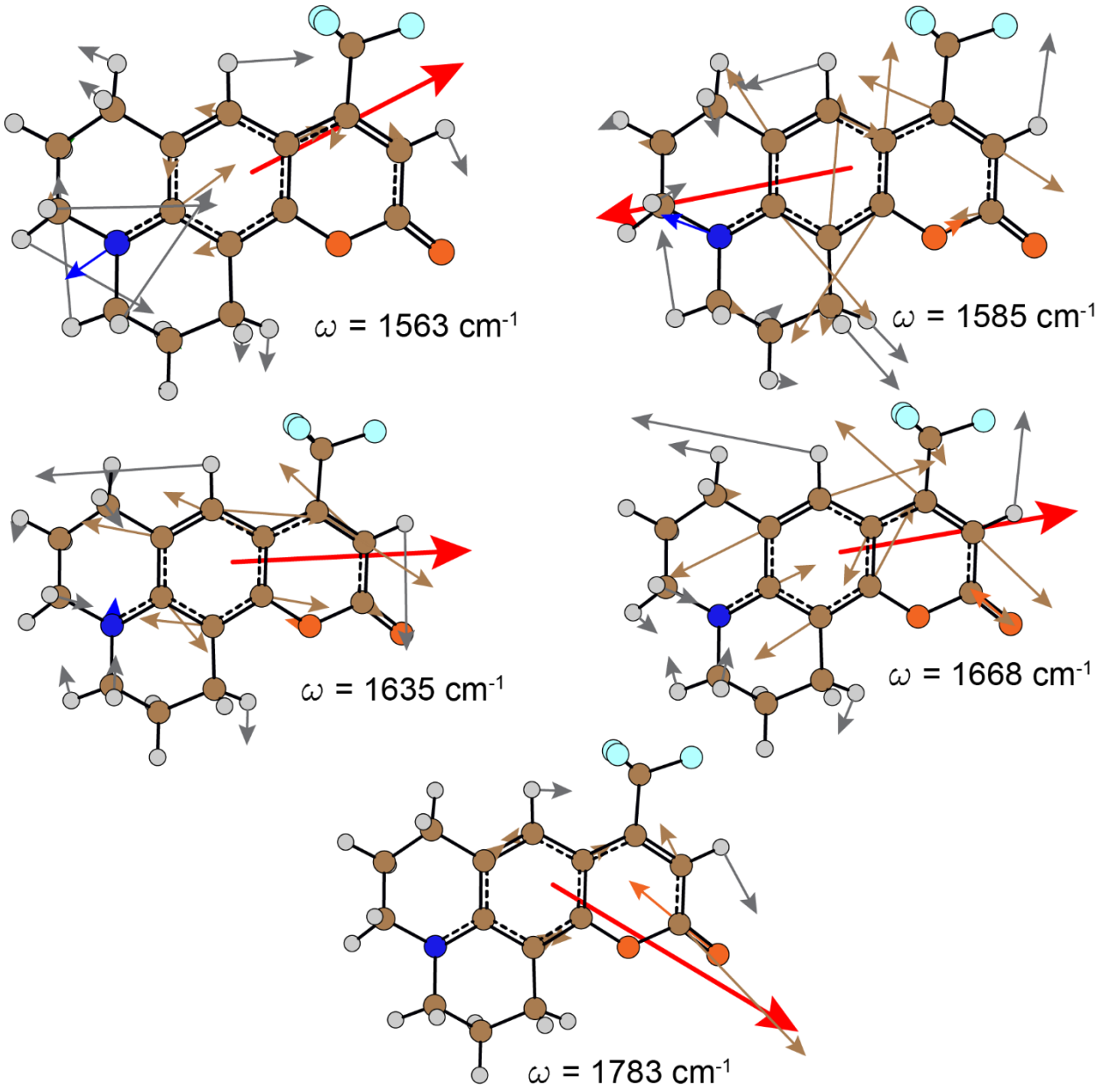


**FIG. S3.3.** Snapshots of the normal modes of coumarin 153 in the spectral window of the IR pump pulse

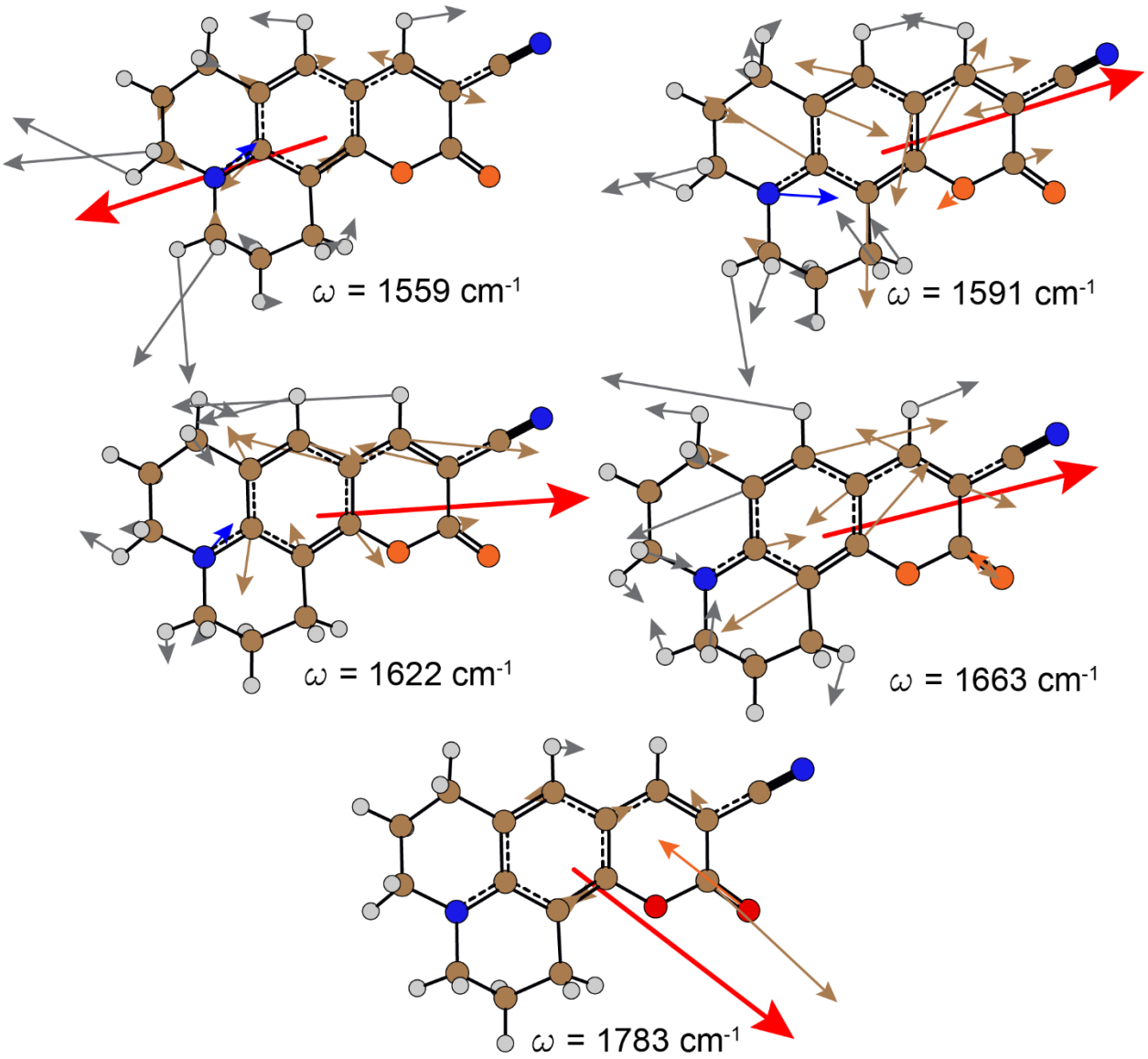


**FIG S3.4.** Snapshots of the normal modes of coumarin 337 in the spectral window of the IR pump pulse

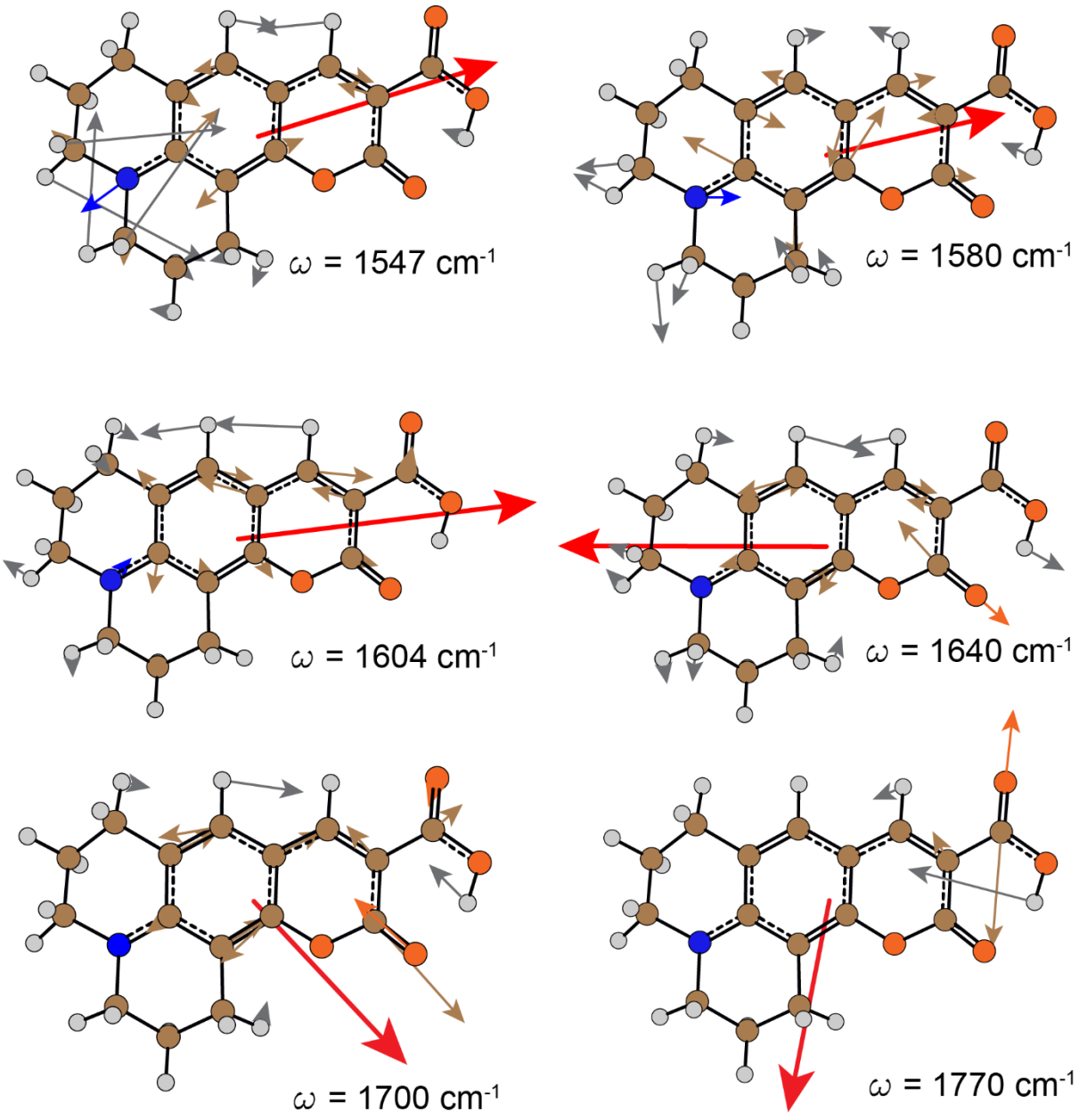


**FIG S3.5.** Snapshots of the normal modes of coumarin 343 in the spectral window of the IR pump pulse. Hydrogen bonding between the -COOH group and the lactone carbonyl is suggested from the synergism between the C=O stretch and the O-H bend.

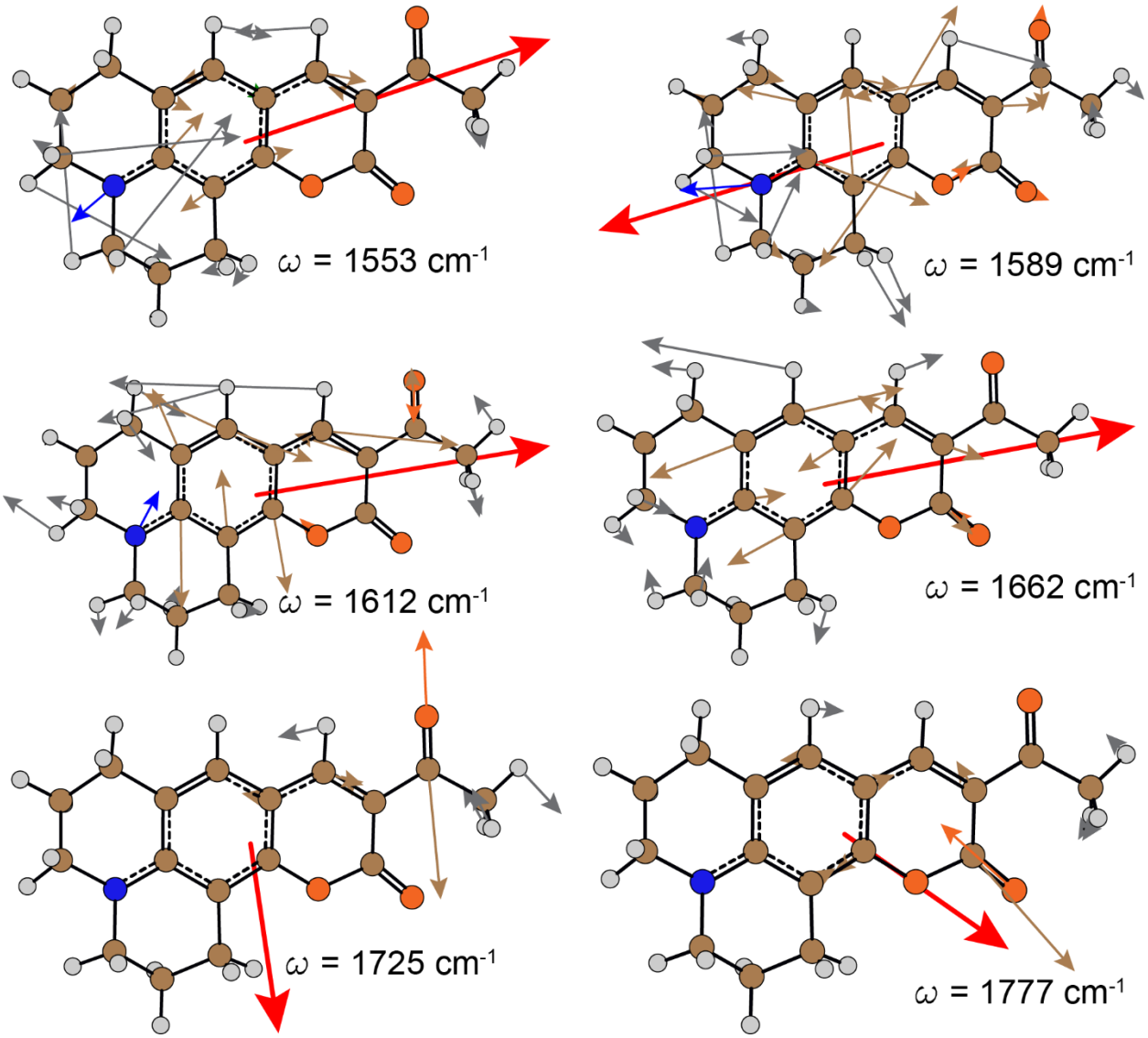


**FIG. S3.6.** Snapshots of the normal modes of coumarin 334 in the spectral window of the IR pump pulse

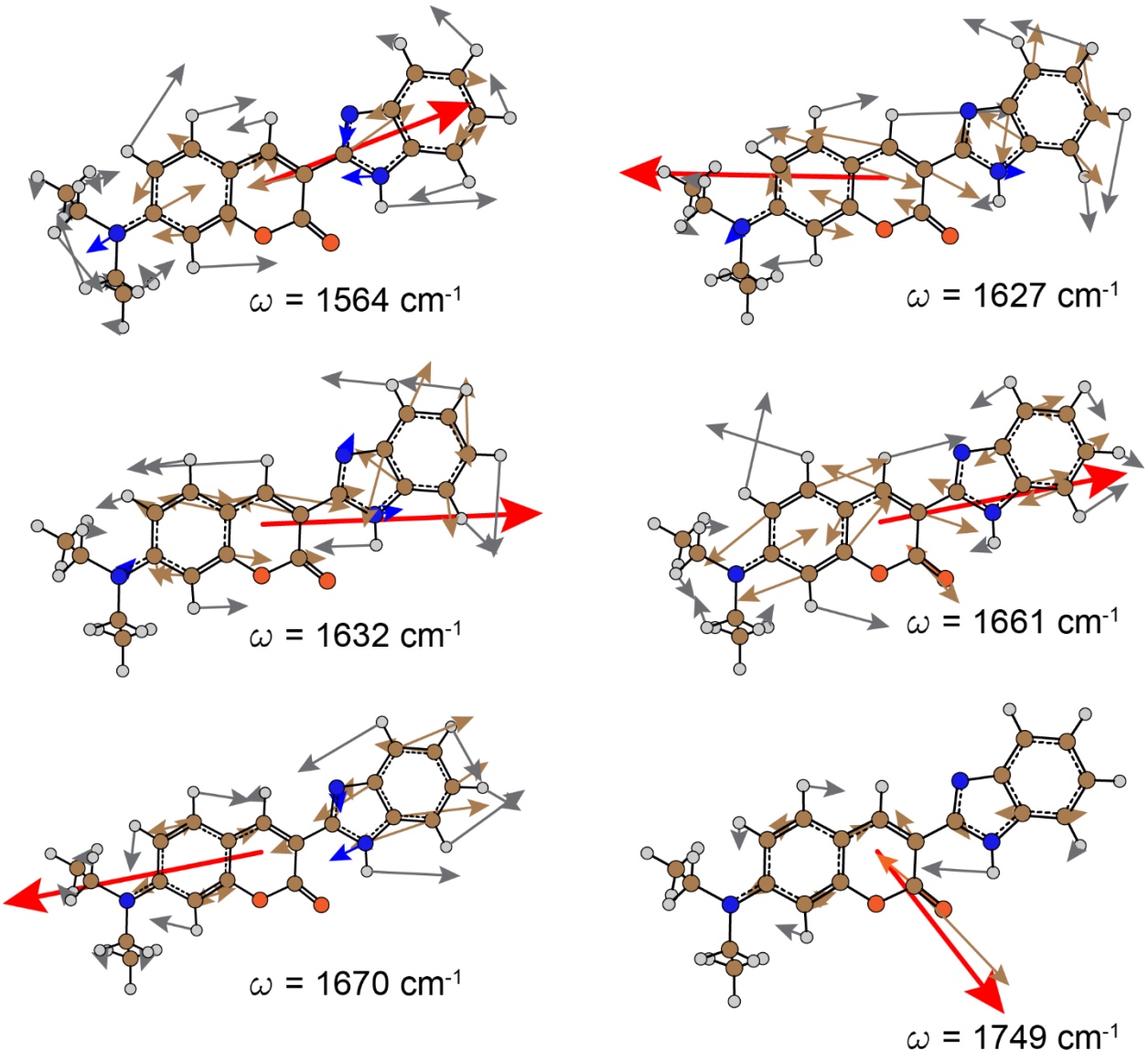


**FIG S3.7.** Snapshots of the normal modes of coumarin 7 in the spectral window of the IR pump pulse

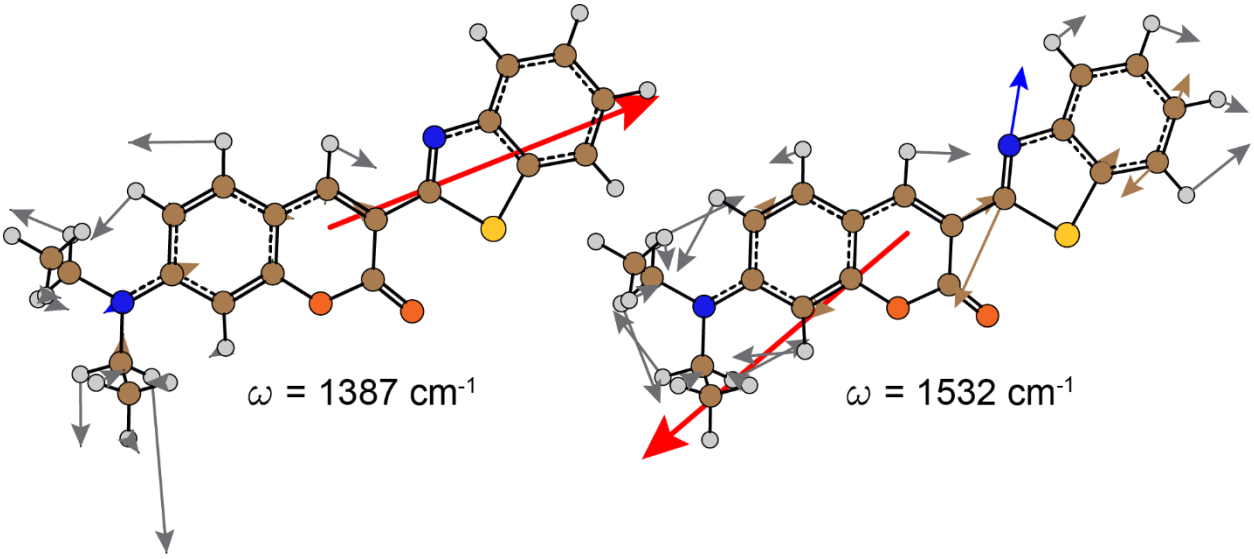


**FIG. S3.8.** Snapshots of the two low frequency ring modes of C6 that demonstrate a non-negligible FEIR activity but lie outside the spectral window of the IR pump. The ring mode with the calculated frequency of 1532 cm-1 is denoted as R4 in Fig. 3 of the main text.

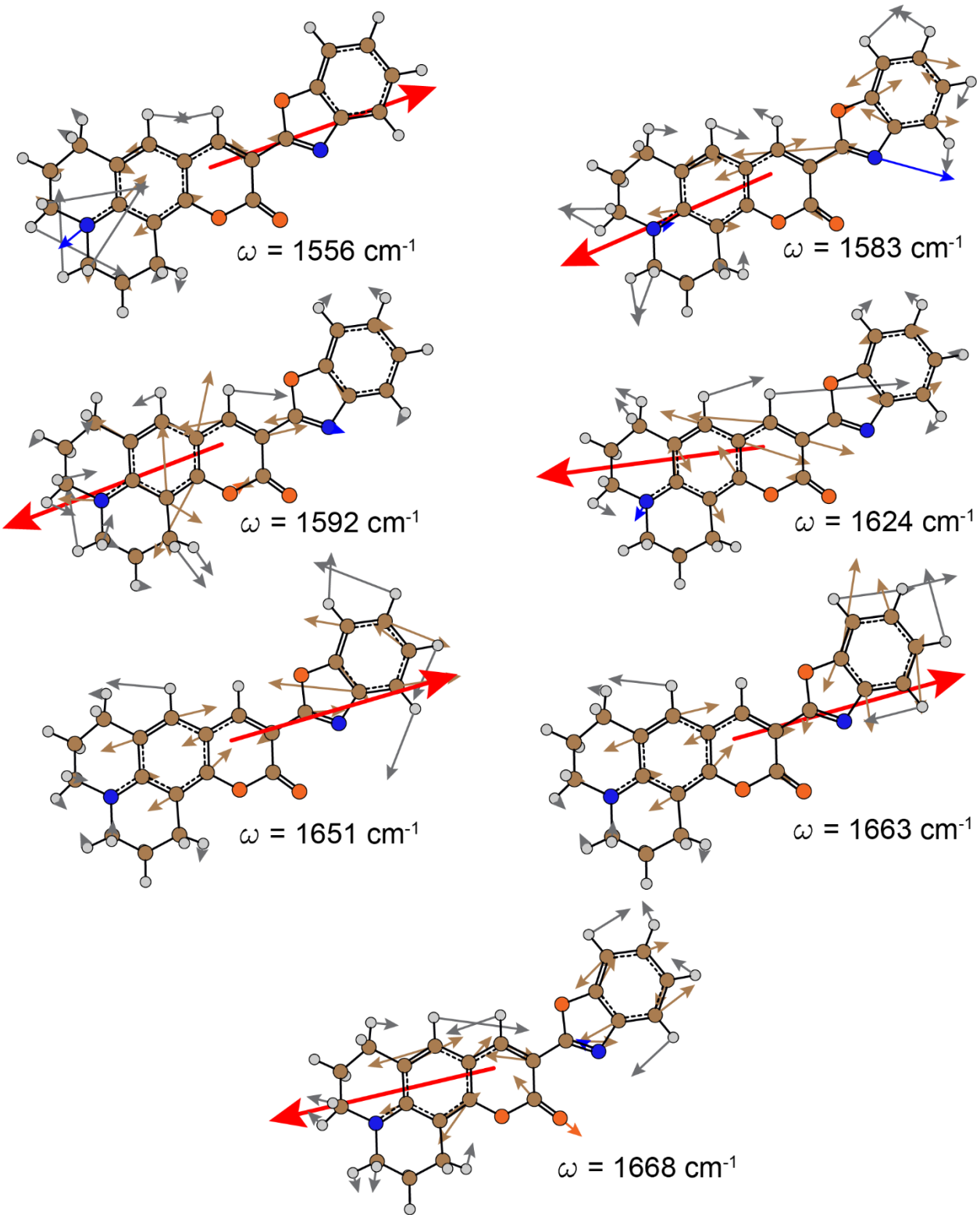


**FIG S3.9.** Snapshots of the normal modes of coumarin 525 in the spectral window of the IR pump pulse. The two ring modes at 1663 and 1668 $cm^{-1}$ jointly contribute to the intensity of the peak appearing at 1622 $cm^{-1}$ in the measured FTIR spectrum presented in ref. 4.

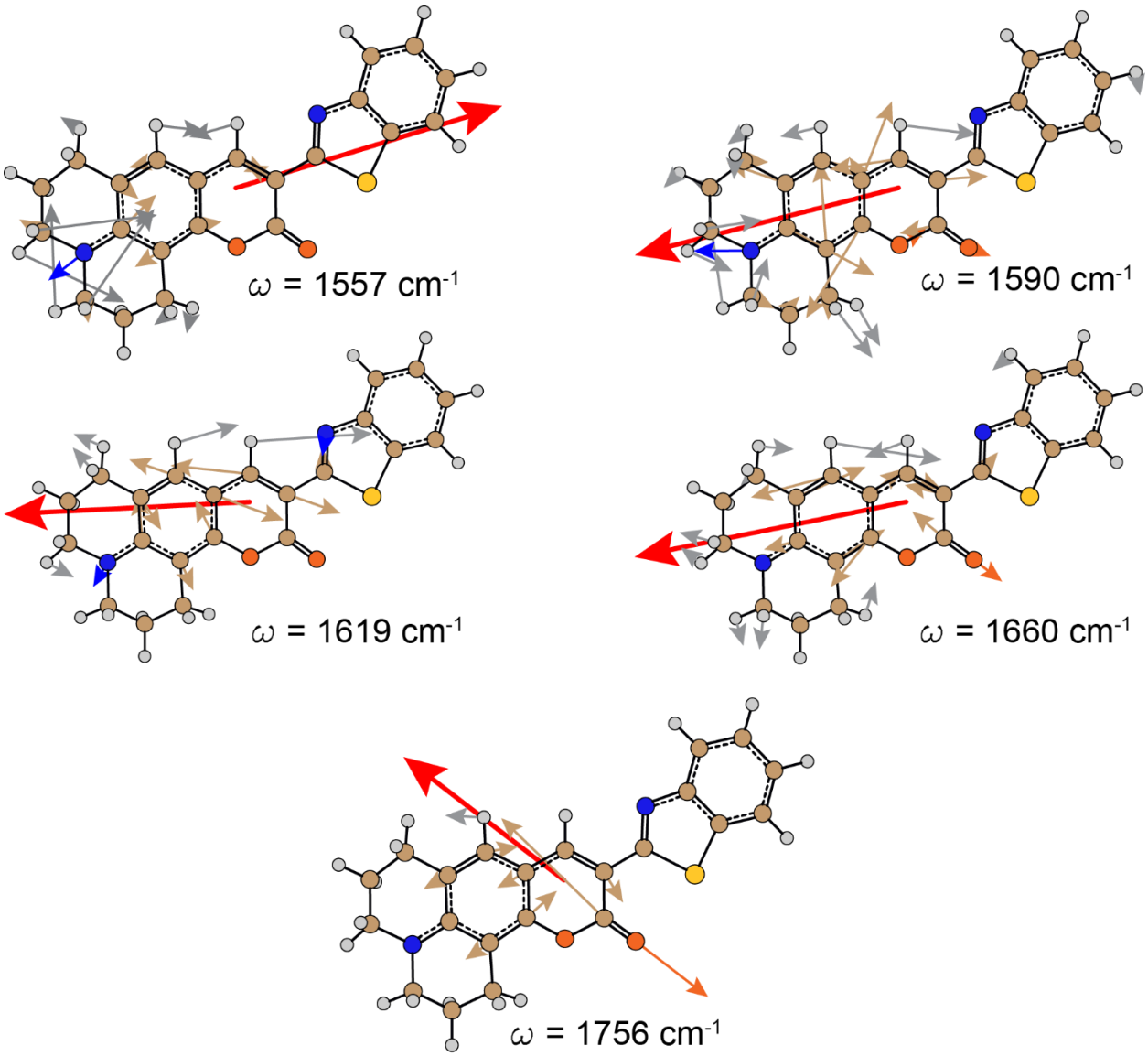


**FIG S3.10.** Snapshots of the normal modes of coumarin 545 in the spectral window of the IR pump pulse.

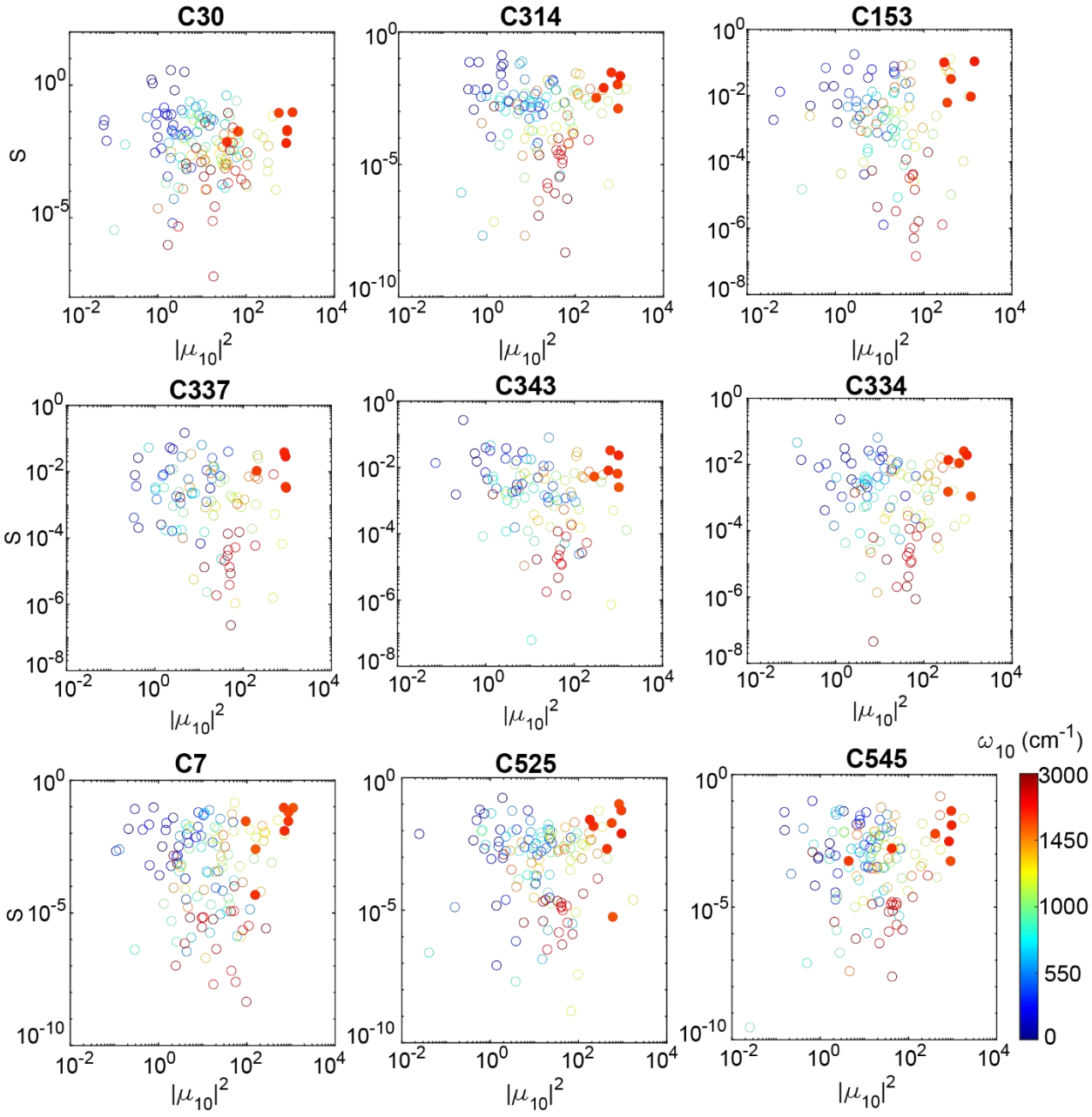


**FIG S3.11.** Correlation between the vibrational transition probabilities and the corresponding Huang-Rhys factors for coumarins. The plot for C6 can be found in the main text (Fig. 6a). Each circle represents a normal mode. The color indicates the corresponding vibrational resonance frequency, and the solid circles indicate the modes within our IR pulse envelope. For all the coumarins, the normal modes excited in FEIR experiments satisfy both the criteria of high transition probability and large Huang-Rhys factors, indicating strong vibronic coupling during the encoding transition. Consequently, coumarins behave as good FEIR probes.

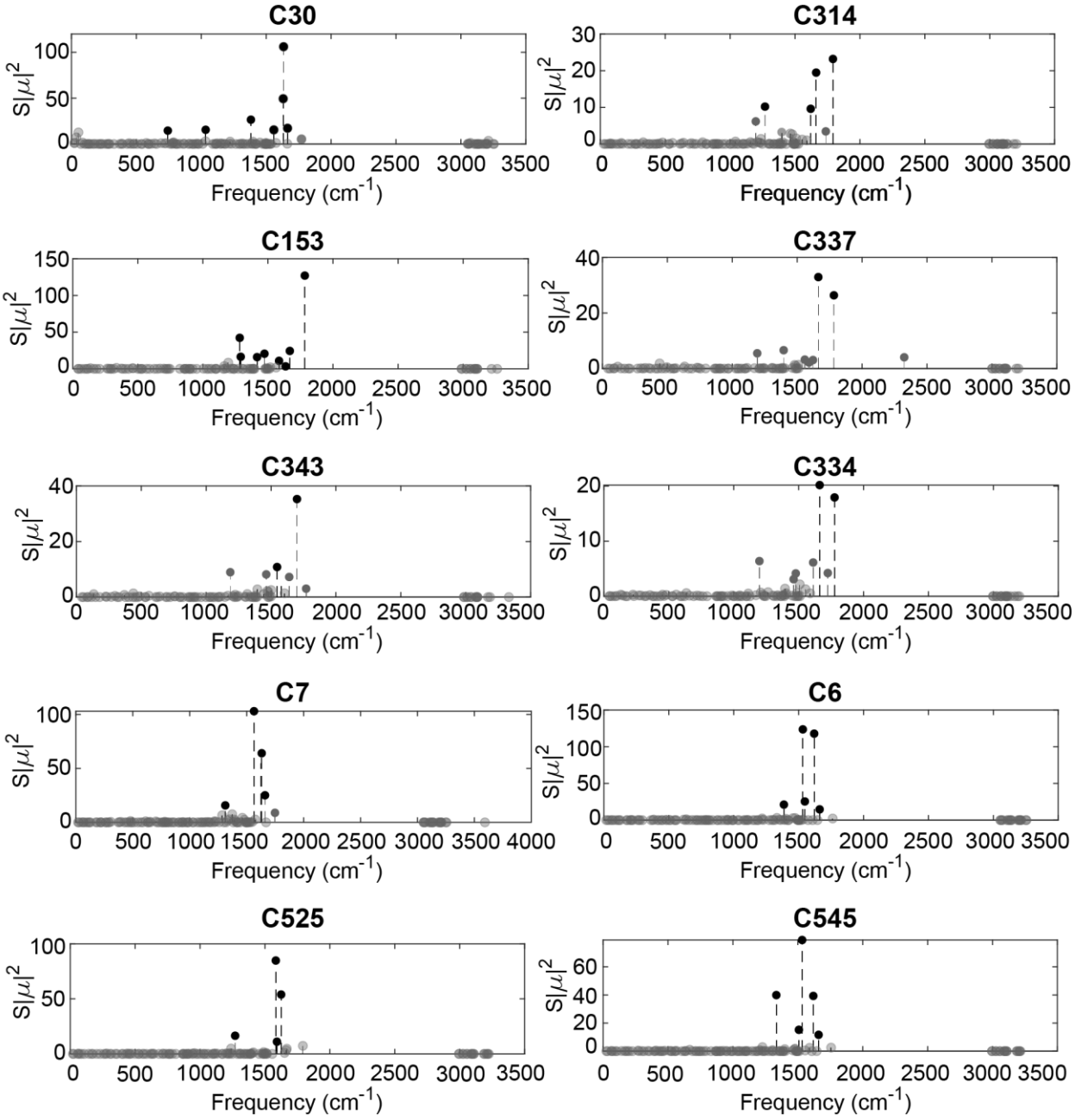


**FIG S3.12.** $S|\mu|^2$ plots of coumarins. The normal modes with $S|\mu|^2$ values > 10 km mol$^{-1}$ are shown in black and the ones shown in grey fall below this threshold.

Table SI below shows the calculated ground state frequencies, vibrational transition dipole moments, and Huang-Rhys factors for the vibrations lying within the spectral window of the IR pump pulse, with $S|\mu|^2 > 10$ km mol$^{-1}$ for all the coumarins studied. The corresponding values for the lactone carbonyls and any other carbonyl mode, if present, are also given, regardless of their $S|\mu|^2$ magnitude.

**Table SI.** Calculated frequencies, vibrational transition dipole moments, and Huang-Rhys factors of the vibrations lying within the IR pump spectral window, for coumarins. (*) indicates the vibrations lie beyond the bandwidth of IR pump, hence, their FEIR cross-sections have not been measured. Normal modes enclosed in [ ] fall within the linewidth of a single peak in the FTIR spectrum.

| Dye | $\omega_{10}$(cm$^{-1}$) | $\|\mu\|^2$(km mol$^{-1}$) | $S$ | Dye | $\omega_{10}$(cm$^{-1}$) | $\|\mu\|^2$ | $S$ |
|---|---|---|---|---|---|---|---|
| | | | | | 1553 | 1168 | 0.001 |
| | 1631 | 552 | 0.089 | | 1589 | 355 | 0.001 |
| **C30** | 1634 | 1126 | 0.094 | **C334** | 1612 | 629 | 0.011 |
| | 1664 | 852 | 0.020 | | 1662 | 804 | 0.025 |
| | 1772 | 812 | 0.006 | | 1725 | 361 | 0.014 |
| | | | | | 1777 | 943 | 0.019 |
| | 1591 | 299 | 0.003 | | 1564 | 1197 | 0.092 |
| | 1621 | 913 | 0.010 | | 1627 | 880 | 0.063 |
| **C314** | 1663 | 659 | 0.029 | **C7** | 1632 | 684 | 0.094 |
| | 1737 | 441 | 0.008 | | 1661 | 871 | 0.029 |
| | 1792 | 1051 | 0.022 | | 1749 | 710 | 0.013 |
| | 1563 | 283 | 0.006 | | *1387 | 741 | 0.029 |
| | 1585 | 344 | 0.032 | | *1532 | 541 | 0.228 |
| **C153** | 1635 | 970 | 0.009 | **C6** | 1548 | 1177 | 0.022 |
| | 1668 | 242 | 0.100 | | 1620 | 1437 | 0.082 |
| | 1783 | 1175 | 0.108 | | 1662 | 1433 | 0.010 |
| | | | | | 1762 | 737 | 0.003 |
| | | | | | 1556 | 595 | $5.6\text{x}10^{-6}$ |
| | | | | | 1583 | 827 | 0.103 |
| | 1559 | 914 | 0.0003 | | 1592 | 566 | 0.020 |
| | 1591 | 203 | 0.011 | | 1624 | 928 | 0.058 |
| **C337** | 1622 | 943 | 0.003 | **C525** | 1651 | 441 | 0.002 |
| | 1663 | 852 | 0.039 | | [1663 | 218 | 0.015 |
| | 1783 | 915 | 0.029 | | 1668] | 180 | 0.026 |
| | | | | | 1792 | 938 | 0.008 |
| | 1547 | 1322 | 0.008 | | 1557 | 898 | $5.4 \times 10^{-4}$ |
| | 1580 | 280 | 0.016 | | 1590 | 403 | 0.006 |
| **C343** | 1604 | 1250 | 0.001 | **C545** | 1619 | 927 | 0.042 |
| | 1640 | 760 | 0.009 | | 1660 | 944 | 0.012 |
| | 1700 | 471 | 0.075 | | 1756 | 828 | 0.003 |
| | 1770 | 750 | 0.004 | | | | |

## S4. Fit results for extracting integrated extinction coefficients of vibrations from FTIRs of coumarins

Each FTIR spectrum is fit to a sum of '$n$' Lorentzian functions, '$n$' being determined by the number of peaks in the spectrum with an $\varepsilon$ value of > 500 M$^{-1}$ cm$^{-1}$:

$$s(\omega) = \sum_{i=1}^{n} \frac{k^{(i)} \cdot b^{(i)}}{(\omega - \omega_0^{(i)})^2 + b^{(i)2}}$$

where, $b$ denotes the width of the Lorentzian function, and $\omega_0$ represents the center frequency. The areas under individual Lorentzians are calculated from the fit parameter '$k$', according to the relation $A = k\pi$. These areas represent the integrated molar extinction coefficients under peaks for individual normal modes, $A = \int \varepsilon(\omega) d\omega$, carrying the unit of $Lmol^{-1}cm^{-2}$ given the frequency is in $cm^{-1}$.

Fig. S4 shows the FTIR spectra of the ten coumarins, along with the respective fits. The reconstructed Lorentzians are shown as shaded areas that represent the integrated extinction coefficients of the respective vibrations. The carbonyl modes for C153, C7 and C525 are spectrally well separated from the ring modes, and are structured, probably due to Fermi resonance with combination of low frequency ring modes. The areas under them are calculated analytically by numerical integration. The lactone carbonyl of C314 shows a doublet centered around 1740 $cm^{-1}$. It is fit to two Lorentzians and the area under them is summed to obtain its total integrated $\varepsilon$.

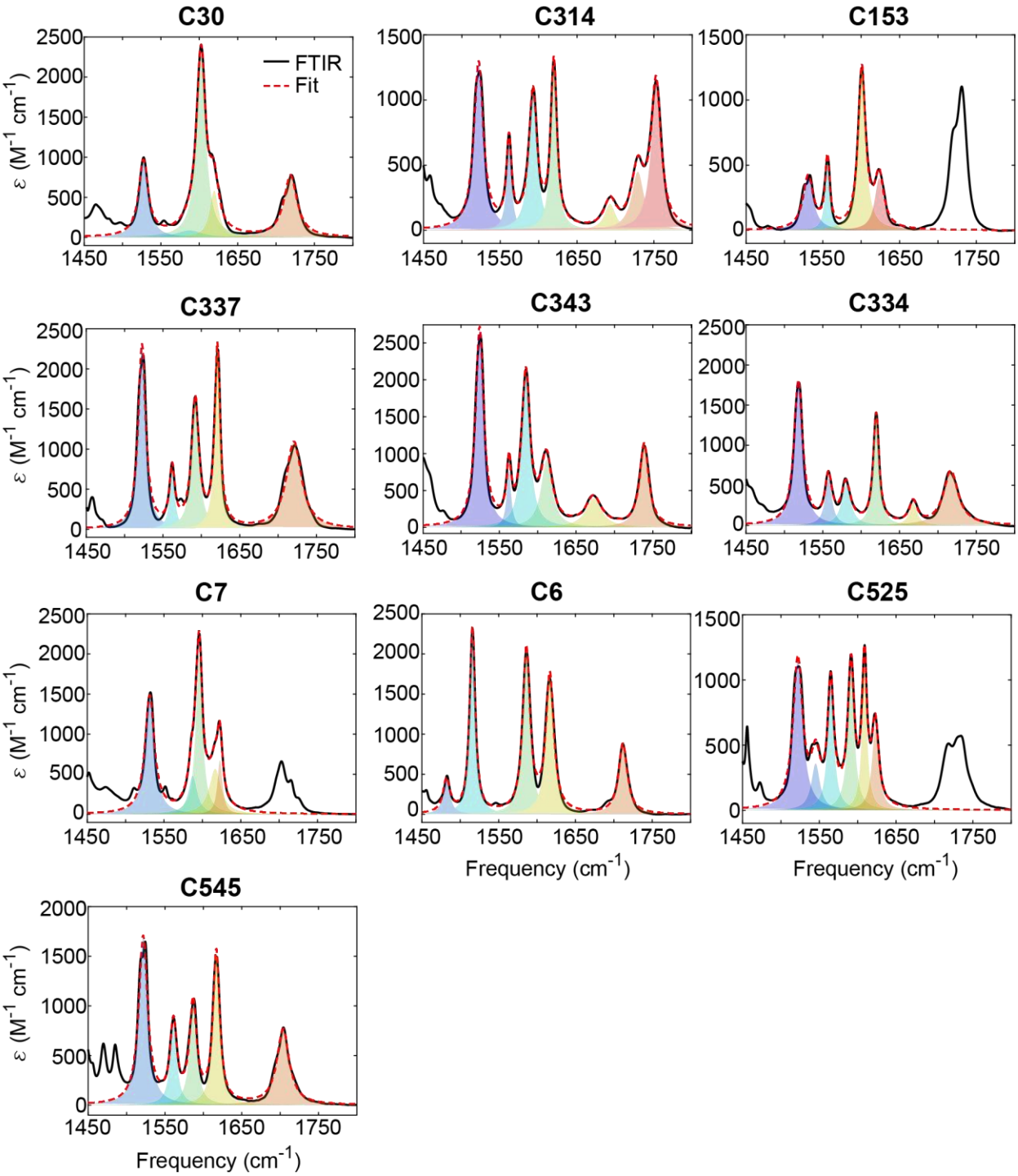


**FIG S4.** FTIRs of coumarins (black) fit to sum of 'n' Lorentzians (dashed red). 'n' is determined by the number of FTIR peaks with $\varepsilon > 500\ Lmol^{-1}cm^{-1}$. The shaded area under the Lorentzians represent the integrated molar extinction coeffient of the individual normal modes. For coumarins whose carbonyl mode is structured (C153, C7, C525), the area is determined analytically by numerical integration. For C314, the lactone carbonyl is a doublet, therefore fit to two Lorentzians, and their areas summed.

## S5. Experimental determination of normal mode anisotropy

Anisotropy values of normal modes were determined from FEIR spectra acquired under relative parallel and perpendicular polarization of IR and visible excitation pulses, using the following equation:

$$r = \frac{S_{\parallel} - S_{\perp}}{S_{\parallel} + 2S_{\perp}}$$

Fig. S5 shows the FEIR spectra collected under parallel (blue) and perpendicular (red) polarization. The anisotropy values are shown as black dots, read off the right Y axis. The value used for each normal mode is the average over the respective linewidth, shown as purple shaded areas. The corresponding DFT-calculated anisotropies are shown as green diamonds.

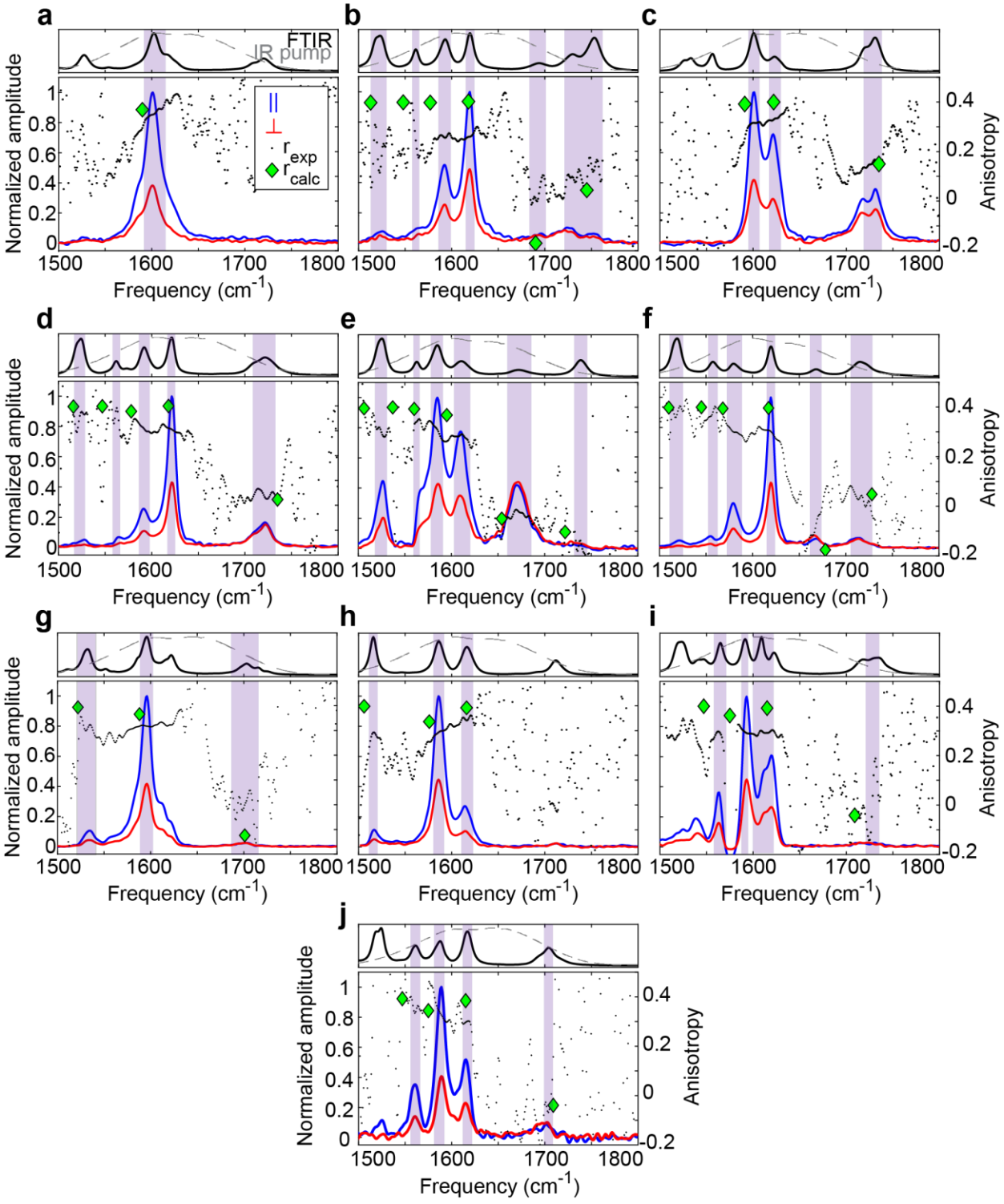


**FIG S5.** Experimental anisotropies of normal modes determined from FEIR spectra acquired with relative parallel (blue) and perpendicular (red) polarization of IR and visible pulses. Anisotropies (black dots) are reported as average over respective linewidths (purple shaded areas). The corresponding FTIR (black) and IR pump spectra (grey) are shown for reference. The DFT-calculated anisotropy values are shown as green diamonds.

## S6. Comparison of experimental and simulated FEIR spectra

Qualitative comparison of experimental and simulated FEIR spectra at $\tau_{enc} = 500\,fs$ and $\tau_{enc} = 0$ are shown in Fig. S6. The correlations between the peak amplitudes are shown in Fig. 9 of the main text. The simulations were conducted following the methodology outlined in Ref. {Whaley-Mayda, 2023 #83}. In this approach, the DFT-calculated matrix elements were utilized as input parameters for the molecular factor, except for the strengths of vibrational transition dipoles. These dipole strengths were determined by fitting the FTIR spectra to a sum of Lorentzian functions, as depicted in Figure S4.

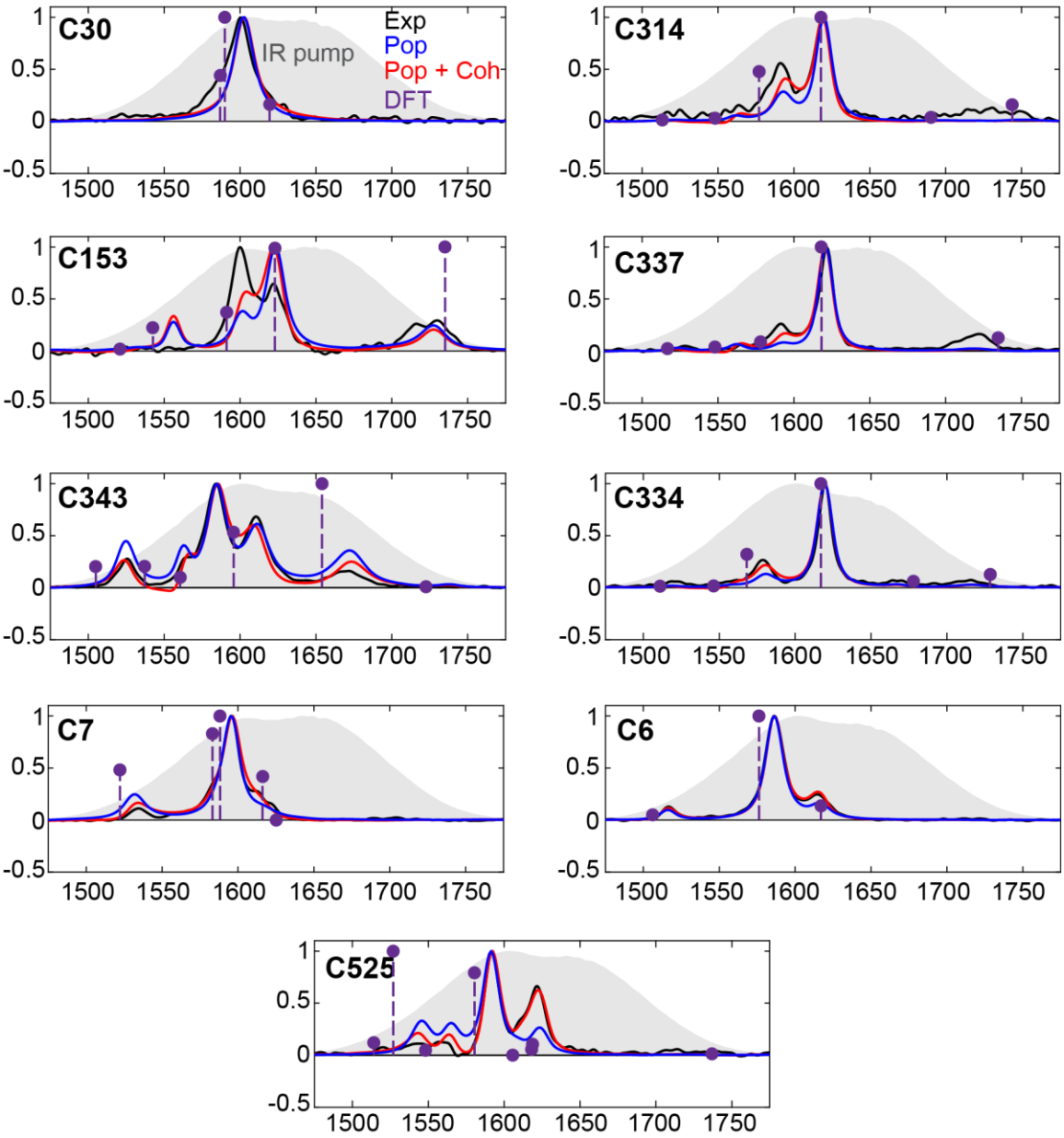

**FIG S6.1.** Qualitative comparison of the experimental and simulated FEIR spectra at $\tau_{enc} = 500\,fs$. The simulations with population pathways are shown in blue, population + coherence pathways in red, and for comparison, the stick spectra derived from DFT calculations (Eq. 8 of main text) are shown in purple. The experimental spectra are shown in black, and the IR pump spectra are shown as grey shaded areas.

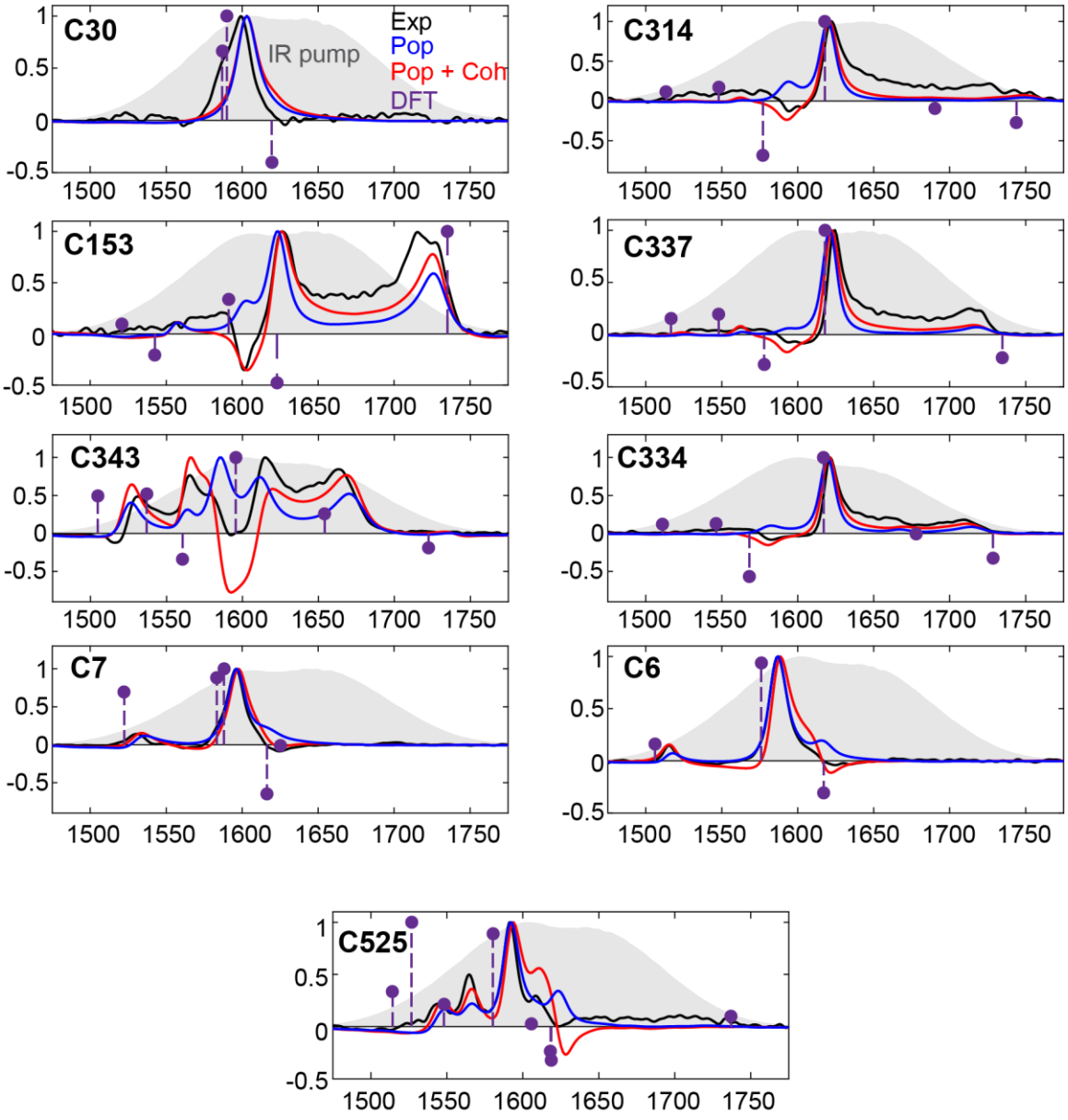


**FIG S6.2.** Qualitative comparison of the experimental and simulated FEIR spectra at $\tau_{enc} = 0$. The simulations with population pathways are shown in blue, population + coherence pathways in red, and for comparison, the stick spectra derived from DFT calculations (Eq. 11 of main text) are shown in purple. The experimental spectra are shown in black, and the IR pump spectra are shown as grey shaded areas.

The simulation results exhibit a high degree of agreement with the experimental spectra, with one notable exception. In the early-time spectra, specifically in the pulse overlap region, the amplitudes of the absorptive continuum for C314, C153, C337, C343, and C334 do not quantitatively match the experimental

data. This discrepancy is attributed to the phenomenon of IR + visible two-photon absorption. The simulations at $\tau_{enc} = 0$ can effectively reproduce the signs of the peaks, commenting on the accuracy of calculations of the relative signs of the FCFs and orientational factors. The correlations of the peak amplitudes at $\tau_{enc} = 500\,fs$ are shown in Fig. 13 of the main text, and those at $\tau_{enc} = 0$ (100fs for experiment) are shown in Fig. S6.3.

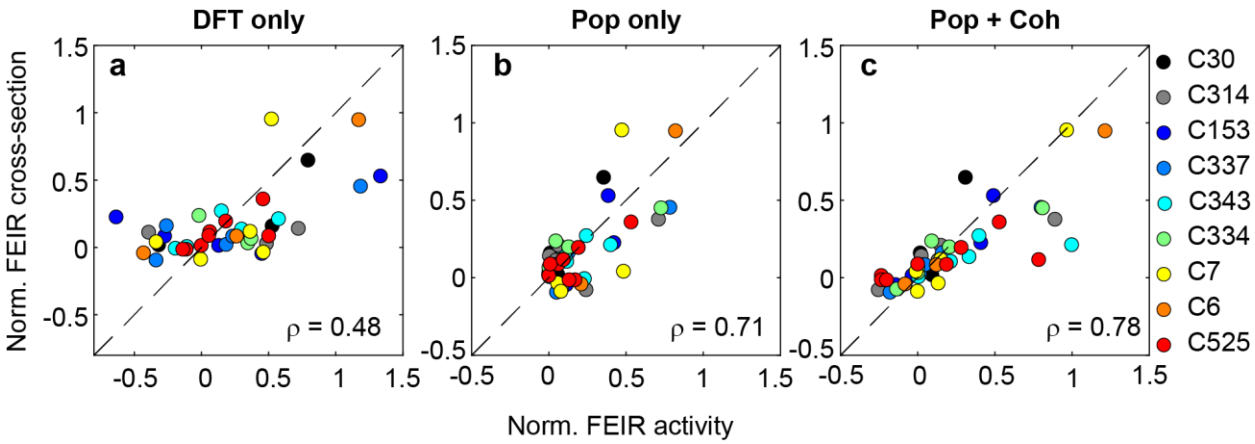


**FIG S6.3.** Effect of vibrational dynamics on the correlation of mode-specific computational predictions to the corresponding experimental FEIR response at $\tau_{enc} = 0$ (100 fs for experiment) . (a) Correlation of the experimental normalized FEIR cross-sections of the vibrations of the coumarins with the normalized mode-specific FEIR activities computed using Eq. (11). (b) Improvement in the correlation with population relaxation and finite pulse effects are included in response function calculations, and DFT-calculated vibrational intensities replaced by values obtained from FTIR spectra. (c) Further slight improvement in correlation upon including the coherence pathways in the simulation.

## S7. Comparison of results using different functionals (Coumarin 6)

**Table SII.** Comparison of energies of the minima of $S_0$ and $S_1$ electronic states, and transition dipole moments of C6 using two different functionals and basis sets

| B3LYP/6-31G(d,p) | | | ωB97XD/Def2TZVP | | |
|---|---|---|---|---|---|
| E ($S_0$) hartree | | E($S_1$) hartree | E ($S_0$) hartree | | E($S_1$) hartree |
| -1431.18 | | -1431.09 | -1430.83 | | -1430.72 |
| $\mu_{eg}$ (x) | $\mu_{eg}$ (y) | $\mu_{eg}$ (z) | $\mu_{eg}$ (x) | $\mu_{eg}$ (y) | $\mu_{eg}$ (z) |
| 4.18 | -0.25 | -0.09 | 4.01 | -0.33 | -0.09 |

To test the dependence of the choice of functional on the calculated FEIR activities, we performed electronic structure calculations on C6 using the long-range corrected functional ωB97XD with Def2TZVP triple zeta basis set. The same functional and basis set were used for calculations on the ground and first

singlet excited states of the molecules. Tables SII summarizes the comparison of the energies in the ground and excited state minima, and electronic transition dipole moments for C6 using B3LYP/6-31G(d,p) (used in the main results) and ωB97XD/Def2TZVP. Table SIII shows the comparison of calculated frequencies of the four normal modes R1, R2, R3 and C=O, their IR intensities, Huang-Rhys factors and relative angles with the electronic transition dipole.

Both levels of theory result in optimized geometries in the ground and excited states with similar energies. The electronic transition dipole moments are also comparable. The new calculations show that there are two normal modes within the linewidth of R3, as compared to 1. If we approximate the calculated anisotropy as the mean of the anisotropies of these two normal modes, it gives a value of 0.31, which is closer to the measured value of 0.27 than the calculated value of 0.39 given by B3LYP/6-31G(d,p) level of theory. This may hint at an improvement over the previous calculations. However, the IR intensity of R1 is underestimated by the long-range corrected functional. Keeping the degree of inconclusivity in mind, and considering that the optimized geometries are very similar for both levels of theory, we retain the results of B3LYP/6-31G(d,p) level of theory in the discussion in the main text.

**Table SIII.** Comparison of frequencies (in $cm^{-1}$), IR intensities (in km/mol), Huang-Rhys factors, and orientational factors of the normal modes of C6 from calculations using B3LYP/6-31G(d,p) (A) and ωB97XD/Def2TZVP (B) levels of theory

| | $\omega_g$ ($cm^{-1}$) | | $\|\boldsymbol{\mu}\|^2$(km/mol) | | S | | θ (relative angle with $\boldsymbol{\mu_{eg}}$) | |
|---|---|---|---|---|---|---|---|---|
| | A | B | A | B | A | B | A | B |
| **R3** | 1548 | 1574<br>1582 | 1177 | 1758<br>345 | 0.022 | 0.093<br>0.224 | 3.2 | 2.5<br>33.2 |
| **R2** | 1620 | 1662 | 1437 | 2158 | 0.082 | 0.195 | 19.0 | 18.3 |
| **R1** | 1662 | 1695 | 1433 | 770 | 0.010 | 0.014 | 6.7 | 1.4 |
| **C=O** | 1762 | 1813 | 737 | 842 | 0.003 | $3.3 \times 10^{-4}$ | 116.0 | 119.4 |

## S8. Computational predictions of FEIR activities of carbonyl modes in coumarins

An ideal single-molecule FEIR probe would involve a vibrational mode that exhibits strong FEIR activity, and is an established reporter of chemical dynamics, such as the carbonyl or nitrile stretch. In our previous discussions, we have focused on predicting molecular and mode-specific FEIR activities. Among the most intense FEIR vibrations found in the brightest coumarins are primarily associated with conjugated C=C stretches, which collectively fall under the category of ring modes. These modes often remain unresponsive to chemical interactions, showing no discernible shifts in vibrational frequencies or intensities that would

qualify them as effective FEIR probes. It is noteworthy that all the coumarins possess a lactone carbonyl group, which resonates in the spectral range of 1660 – 1730 $cm^{-1}$. Additionally, some coumarins, such as C314, C343, and C334, feature another carbonyl group as a ring substituent. In this context, we aim to compare the predictions of the FEIR activities associated with these carbonyl groups to the experimentally measured FEIR cross-sections across the coumarin series.

In Fig. S8, we show the comparison between the DFT-calculated FEIR activities of the carbonyls (Eq. 6 without IR pump scaling) of all coumarins except C30 (unable to resolve carbonyl peak from noise), and their corresponding experimental FEIR cross-sections. The latter are obtained as fractional values of the overall FEIR cross-sections of the molecules, determined from two-pulse transients, averaged over the encoding delay range of 400 – 800 fs. The fractions are determined as a ratio of the area under the carbonyl peak, obtained by fitting the peak to a Gaussian function to the total area under the spectrum. The spectrum used is also an average over the same range of encoding delays. These values are additionally normalized by the relative intensity of the IR pump pulse over the carbonyl, and the electronic lineshape value at $\omega_{vis} + \omega_{IR}$. While the correlation between the two quantities is not remarkable (fit shown as dashed line; $R^2$ = 0.91), there are a couple of aspects worth noting. First, there are consistent predictions of stronger FEIR activities of lactone carbonyls (circles) than the substituent carbonyls (rhombi). Furthermore, the model also predicts that C153 has the brightest lactone carbonyl, whose large FEIR activity is primarily attributed to its large Huang-Rhys factor as compared to the others (even larger than the C153 ring modes), and a strong vibrational transition dipole; in other words, a large $S|\mu|^2$. The displacement of the excited electronic potential along the normal coordinates of a mode may have a correlation with the change in the electron density over the mode during the $\pi - \pi^*$ transition, as suggested tangentially in the literature. We leave it at this speculation, due to the lack of any theory that suggests that these two quantities are indeed correlated.

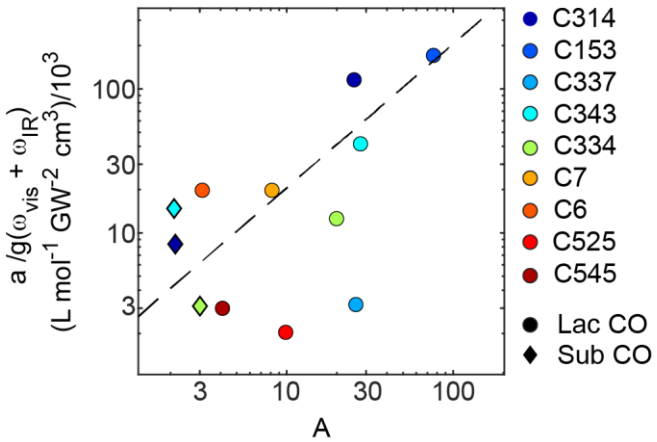

**FIG S8**. Correlation of the FEIR cross-sections of carbonyl modes in the coumarins to their predicted FEIR activities. The predictions suggest that lactone carbonyls systematically have larger FEIR activities than substituent carbonyls. Furthermore, the model correctly predicts the largest FEIR activity of C153 lactone carbonyl.

# References


[1] P. T. Ruhoff, "Recursion relations for multi-dimensional Franck-Condon overlap integrals", Chemical Physics **186**, 355-74 (1994).

[2] F. Santoro, A. Lami, R. Improta, and V. Barone, "Effective method to compute vibrationally resolved optical spectra of large molecules at finite temperature in the gas phase and in solution", Journal of Chemical Physics **126**, (2007).

[3] T. E. Sharp, and H. M. Rosenstock, "Franck—Condon Factors for Polyatomic Molecules", The Journal of Chemical Physics **41**, 3453-63 (1964).

[4] L. Whaley-Mayda, A. Guha, and A. Tokmakoff, "Resonance conditions, detection quality, and single-molecule sensitivity in fluorescence-encoded infrared vibrational spectroscopy", The Journal of Chemical Physics **156**, 174202 (2022).